

1 **Partial Melting of a Depleted Peridotite Metasomatized by a MORB-Derived Hydrous**
2 **Silicate Melt – Implications for Subduction Zone Magmatism**

4 Michael Lara^{1*}

5 Rajdeep Dasgupta¹

6 ¹Department of Earth, Environmental and Planetary Sciences, Rice University, 6100 Main Street,
7 MS 126, Houston, TX 77005

8 *Corresponding author: mall5@rice.edu

10 **Abstract**

11 Recent geodynamic models and geothermometers suggest that slabs in intermediate to hot
12 subduction zone cross the water-saturated basalt solidus, indicating that hydrous silicate melts are
13 important agents of mass transfer from slab to mantle wedge beneath arcs. Yet the effects of
14 basaltic crust-derived hydrous melt fluxing on mantle wedge melting are poorly known. Here we
15 present the melting phase relations of a depleted peridotite + a MORB-derived hydrous silicate
16 melt at a melt:rock mass ratio of 0.1 and 0.05 (3.5 and 1.7 wt. % H₂O, respectively) to simulate
17 fluid-present partial melting of a depleted peridotite, which has been metasomatized by a hydrous
18 silicate melt derived from subducting basaltic crust. Experiments were performed at 2-3 GPa and
19 900-1250 °C in a piston cylinder, using Au and Au₇₅Pd₂₅ capsules. Amphibole (7-10 wt%) is stable
20 up to 1000 °C at 2 and 3 GPa coexisting with an assemblage dominated by olivine and opx and
21 with minor fractions of cpx and garnet at 3 GPa. The apparent fluid-saturated solidus of our bulk
22 composition is located at 1000-1050 °C, coinciding with the exhaustion of amphibole at 2 and 3
23 GPa. Amphibole is exhausted between 0 and 5 wt.% melting at 2 and 3 GPa and dominates the
24 melting reactions in this melting interval along with opx, generating SiO₂ and Al₂O₃-rich, and
25 FeO*- and MgO-poor primitive andesites under fluid-saturated conditions. The melting reactions
26 during low-degree, fluid-saturated melting are incongruent, consuming opx and producing olivine
27 + SiO₂-rich melts and is observed over a wide range of starting compositions and pressures from
28 this study and others. As extent of melting increases and the free fluid phase is consumed, a
29 spectrum of basaltic andesites to basanites are produced. Comparison of experimental partial melts
30 from this and other hydrous peridotite melting studies with natural primitive arc magmas suggests
31 that melting of peridotites with varying bulk compositions but with 2.5 – 4.2 wt.% H₂O can

32 reproduce the major oxide spread and trends of primitive arc magmas globally. From this
33 comparison, it is clear that differences solely in the pressure of hydrous mantle melting, where the
34 partial melts are fluid-under saturated, can account for the first order trends observed in
35 experimental and natural data, with differences in temperature and composition contributing to the
36 compositional spread within these trends. The ubiquity of andesite genesis over a wide range of
37 pressures and bulk compositions during aqueous fluid-saturated melting suggests that the relative
38 rarity of primitive andesitic melt flux through the crust could be related to the fact that such melts
39 are only produced at the base of the mantle wedge where temperatures are relatively low. As fluid-
40 saturated andesitic melts ascend into the hotter core of the mantle wedge, they are likely consumed
41 by higher-degree, fluid-undersaturated melting generating more common hydrous basaltic melts.

42
43 **Keywords** subduction zones, arc magmas, hydrous peridotite melting, MORB-eclogite-derived
44 hydrous melt, high-Mg andesite
45
46

47 1. INTRODUCTION

48

49 Mass transfer mediated by fluids in subduction zones has played a fundamental role in the
50 chemical differentiation of Earth. The first step in this process is the transfer of fluids from the
51 subducting lithosphere to the mantle wedge above, inducing partial melting and generating primary
52 melts in equilibrium with the mantle (Manning, 2004). The composition of primary melts then
53 variably evolves to more felsic compositions by crystal fractionation and or crustal assimilation
54 during their ascent, operating as the second step of mass transfer to the surface and serving as a
55 mechanism by which felsic continental crust is formed (Kay and Kay, 1991). In the general view
56 of this two-step model, the fluids in the former are dilute aqueous solutions while the primary
57 melts in the latter are basalts. However, both of these views may not generally apply to all modern
58 and ancient subduction zones.

59 Recent geodynamic models (van Keken et al., 2002, Syracuse et al., 2010), and
60 geochemical methods (Hermann and Spandler, 2008, Plank et al., 2009,, Cooper et al., 2012)
61 applied to modern subduction zones suggest that many slab surface *P-T* paths are likely to cross
62 the aqueous fluid-saturated basalt and pelitic sediment solidi at sub arc depths. A requirement for
63 such melting within the thermal structure of modern subduction zones is the availability of free
64 water in the crustal package, most of which is exhausted in the fore-arc at temperatures below the

water saturated solidus (Tatsumi et al., 1986,, Hermann et al., 2006, Hacker, 2008, van Keken et al., 2011). However, the breakdown of chlorite and/or serpentinite in the subducting mantle lithosphere near sub-arc depths flushes the overlying crustal package with aqueous fluids and induces flux melting of silicate sediments and eclogite (Prouteau et al., 1999, Poli and Schmidt, 2002, van Keken et al., 2011, Spandler and Pirard, 2013, Walowski et al., 2015, 2016). While slab melting may presently be restricted to the intermediate to hottest subduction zones, it may have been a more common process operating throughout much of Earth's history. In particular, many Archean tonalite-trondhjemite-granodiorite (TTG) terrains share similar major and trace element characteristics with partial melts of hydrous mid ocean ridge basalts (MORB), leading to the interpretation that extensive slab melting in Archean subduction zones facilitated by higher mantle potential temperatures played a crucial role in the generation of continental crust (Martin, 1986, 1993, Drummond and Defant, 1990, Rapp et al., 1991, 1999, 2003, Drummond et al., 1996). Therefore, hydrous silicate melts are likely important agents of mass transfer from subducting slabs to the mantle wedge in modern and ancient subduction zones.

Given the realized importance of slab melting in subduction zones throughout Earth's history, numerous experimental studies have investigated the partial melting behavior of hydrous MORB and sediments at conditions relevant to subduction zones (High P , Low T). These studies demonstrate that near solidus melting of both crustal lithologies produces hydrous dacitic to rhyolitic melts containing 10-35% dissolved H_2O with sediment melts being more potassic relative to partial melts derived from hydrous MORB (Ryabchikov et al., 1996, Prouteau et al., 2001, Hermann and Green, 2001, Kessel et al., 2005, Hermann and Spandler, 2008, Sisson and Kelemen, 2018) (Fig. 1). Hydrous silica-rich melts liberated from the subducting slab, being far out of equilibrium with peridotite, react with peridotite in the mantle wedge above forming metasomatic phase assemblages and hybridized melts. This process is recorded in several mantle wedge xenoliths containing hydrous minerals, such as phlogopite and amphibole, and silica-rich glass (Kepezhinskas et al., 1995, Schiano et al., 1995, Drummond et al., 1996, Ertan and Leeman, 1996, Kilian and Stern, 2002, Ishimaru et al., 2006). Many arc lavas also show He, Hf, Nd, Pb, Sr isotopes and trace elements patterns indicative of slab melt components present in their source regions. (Defant and Drummond, 1990, Yogodzinski and Kelemen, 1998, Kelemen et al., 2003, Cai et al., 2014, Kimura et al., 2014, Walowski et al., 2015, Yogodzinski et al., 2015).

While slab melting likely occurred in ancient subduction zones and continues to occur in

96 many modern subduction zones, the fate of slab melts as they are transported through and interact
97 with the mantle wedge is enigmatic. The complexity of these interactions arises from the large
98 number of parameters involved. Infiltrating fluid and peridotite composition, melt/rock or
99 fluid/rock ratio, style of transport, pressure and temperature all need to be considered, and the
100 range within these parameters may result in a wide variety of metasomatic phase assemblages and
101 hybrid melt compositions. Constraining the influence that these parameters have on both mantle
102 wedge metasomatism and the composition of primary arc magmas has therefore been the subject
103 of many experimental studies simulating fluid/rock reactions at mantle wedge conditions.

104 Peridotite + H₂O is the most extensively studied fluid/rock system. Experiments show that
105 partial melting of peridotite in the presence of water at low pressures (≤ 1.5 GPa) can produce
106 silica-rich primary melts (SiO₂ > 55 wt.%) at temperatures ~200 °C cooler than the dry peridotite
107 solidus (Green, 1973, 1976, Mysen and Boettcher, 1975b, Kawamoto and Holloway, 1997, Hirose,
108 1997, Grove et al., 2006, Mitchell and Grove, 2015). Past studies (Kushiro et al., 1972, Till et al.,
109 2012) reported silica-rich melts in equilibrium with peridotite at high pressures (>1.5 GPa);
110 however, the role of quench modification as discussed in Green (1973, 1976) was not addressed
111 and these results remained controversial (Green, 2012). Recently, Grove and Till (2019) found that
112 low-degree melting of peridotite fluxed with H₂O + alkalis produces SiO₂-rich melts at 3.2 GPa.
113 These results indicate that andesitic primary melts can form by direct partial melting of the mantle
114 wedge at pressures of 1.0 - 3.2 GPa. Interestingly, the rare occurrence of high Mg# andesites in
115 some modern arcs, which are similar in composition to the average continental crust, suggest that
116 some andesitic lavas erupted in arcs may have undergone minimum alteration since last being in
117 equilibrium with the mantle (Gill, 1981). This has led to the interpretation that high Mg# andesites
118 may form by direct partial melting of the slab and/or mantle wedge (Kelemen, 1995.). Given the
119 importance of slab melts as agents of mass transfer discussed above, other experimental studies
120 have been conducted using peridotite which has been variably metasomatized by sediment and
121 MORB-derived hydrous partial melts to constrain the full range of phase assemblages and partial
122 melt compositions that are generated in the mantle wedge.

123 Two previous studies have investigated partial melting of peridotite fluxed with K-rich
124 hydrous sediment melts at a fixed melt/rock ratio of 0.25 at 2-4 GPa and 850-1350 °C (Pirard and
125 Hermann, 2015, Mallik et al., 2015). Furthermore, Mallik et al., (2016) explored the effect of

126 variable bulk H₂O content on such sediment melt-peridotite interactions. These experiments
127 contained large modal abundances of alkali rich hydrous phases (amphibole and phlogopite)
128 during melting and produced ultrapotassic melts. Pirard and Hermann (2015) and Mallik et al.,
129 (2015, 2016) used depleted and fertile peridotite, respectively, for the mantle component of their
130 starting compositions and produced phonolitic to nepheline normative ultrapotassic melts with
131 compositions similar to some rare arc lavas, yet much more alkali-rich than both the majority of
132 arc lavas and the bulk composition of the continental crust.

133 Other studies have investigated the interaction between alleged MORB-derived melt and
134 peridotite; however, the metasomatic agents used in these studies are either derived from K-rich
135 MORB or assumed to be similar to alkali rich granites (Prouteau, 2001, Rapp et al., 1999, Sen and
136 Dunn, 1994, Sekine and Wyllie, 1982). The latter assumption may not be valid because MORB-
137 derived melts are generally K-poor, an important consideration given the control of alkali content
138 on the stability of hydrous minerals and the composition of hybridized melts. Moreover, these
139 studies were performed at high melt/rock ratios (>1) resulting in felsic bulk compositions rich in
140 SiO₂, Al₂O₃, Na₂O, and K₂O (Fig. 1), and produced hydrous rhyolitic to trachytic melts often in
141 equilibrium with an olivine-free residua. Although such high melt/rock ratios may be locally
142 feasible directly along the slab-wedge interface or during melt focusing, once slab melts migrate
143 upwards through the base of the mantle wedge, the environment is likely to be dominated by
144 depleted peridotite as indicated by several natural samples of sub arc xenoliths (Maury et al., 1992,
145 Arai et al., 2004, Ishimaru et al., 2006, Halama et al., 2009, Morishita et al., 2011, Pirard et al.,
146 2013). Therefore, the reaction between MORB-derived melt and depleted peridotite needs to be
147 investigated using realistic MORB-derived melt compositions and in a peridotite dominated
148 system.

149 Here, we characterize the phase and melting relations of a depleted peridotite,
150 metasomatized by a K-free hydrous MORB-derived melt. Experiments were run at 2-3 GPa and
151 900-1250 °C at a melt/rock mass ratio of 0.1 and 0.05. Due to the low melt/rock ratios, our bulk
152 compositions on an anhydrous basis are similar to a depleted peridotite with minor enrichments in
153 SiO₂, Al₂O₃, and Na₂O yet still more depleted in CaO and Al₂O₃ than fertile peridotite (Fig. 1).
154 Most previous hydrous peridotite melting studies were performed using fertile peridotites (Fig. 1),
155 that is peridotites rich in CaO and Al₂O₃. Thus, aside from gaining insights into the phase and

156 melting relations of a mantle wedge fluxed with a MORB-derived hydrous silicate melt, this study
157 also offers a look into the phase and melting relations of the depleted peridotite endmember during
158 hydrous mantle melting.

159

160

161 **2. Methods**

162

163 **2.1 Starting Materials**

164

165 The slab derived melt composition (RK89) used in this study is a hydrous partial melt of a K-free
166 basalt (TB-1) representative of a typical MORB composition (Schmidt and Poli, 1998). RK89 was
167 generated at 4 GPa, 900 °C in the study of Kessel et al., (2005), hereafter referred to as MM. The
168 peridotite composition (AVX-51) used in this study is representative of an unmetasomatised
169 depleted mantle wedge peridotite from the Kamchatka arc (Rapp et al., 1999, Kepezhinskas et al.,
170 1995), hereafter referred to as DP. Bulk compositions used in this study are homogenous mixtures
171 consisting of 90 wt.% DP and 10 wt.% MM (DP + 10% MM) and 95 wt.% DP and 5 wt.% MM
172 (DP + 5% MM). DP + 10% MM and DP + 5% MM are used to simulate a depleted mantle wedge
173 infiltrated by a hydrous slab derived melt via porous flow at a melt-rock ratio of 0.1 and 0.05,
174 respectively (Table 1, Fig 1). The bulk water contents of DP + 5% MM and DP + 10% MM are
175 1.76 and 3.5 wt.%, respectively. The starting powder was synthesized using reagent-grade oxides
176 (SiO_2 , TiO_2 , Fe_2O_3 , MnO , MgO), carbonates (CaCO_3 , Na_2CO_3 , K_2CO_3), and hydroxides (Al(OH)_3 ,
177 Mg(OH)_2). To minimize contamination by water adsorption, SiO_2 , TiO_2 , and MgO were heated
178 overnight at 1000 °C, Fe_2O_3 , CaCO_3 , Na_2CO_3 , and K_2CO_3 at 800 °C, and MnO at 300 °C. The
179 oxides and carbonates were mixed in the proportions of the calculated starting composition and
180 were ground under ethanol for 1 hour in an agate mortar. Once the ethanol had evaporated, the
181 mixture was fired in a Deltech CO-CO₂ gas mixing furnace at $\log\text{O}_2 \sim \text{FMQ} - 2$ for 24 hours to
182 reduce Fe^{3+} to Fe^{2+} and to decarbonate the carbonate powders. Al(OH)_3 and Mg(OH)_2 was then
183 added to the reduced powder in the amount necessary to yield the desired Al_2O_3 and MgO
184 concentrations and to introduce the desired level of bulk water. The reduced powder plus the added
185 hydroxides were then ground and mixed under ethanol for 1 hour in an agate mortar. This powder
186 was collected in a glass vile and stored at 110 °C in a drying oven.

187

188 **2.2 Experimental Procedure**

189

190 All experiments were performed using a half-inch piston cylinder apparatus in the Experimental
191 Petrology Laboratory at Rice University at pressures of 2-3 GPa and temperatures of 900-1250 °C.
192 The starting material was packed into 3 mm outer diameter Au₇₅Pd₂₅ capsules for experiments at
193 1200 - 1250 °C and packed into 2 mm outer diameter Au capsules for all other experiments at 900
194 - 1200 °C and welded shut using a graphite welder or a PUK welding machine. The capsule was
195 then inserted into a drilled hole within a 17 mm long MgO insert, which is nestled in the center of
196 the pressure assembly. The assembly of each experiment consisted of MgO inserts surrounded by
197 a graphite furnace, all enclosed in a BaCO₃ sleeve in which the outside is lined with lead foil to
198 reduce friction. The pressure and temperature calibration for the assembly is that presented in
199 Tsuno and Dasgupta (2011), which applies a - 11% friction correction for pressure. The
200 temperature was monitored with a Type C thermocouple, which is accurate within ± 10 °C
201 accounting for the thermal gradient across the assembly. The pressure was manually monitored
202 for the first couple hours, followed by the employment of a pressure controller to keep the pressure
203 within ± 0.02 GPa of the target pressure. The experiments were first pressurized and then heated
204 up to the desired temperature at 100 °C/min. The experiment duration ranged from 96 to 169 hours
205 and the experiments were quenched by cutting the power to the graphite furnace and allowing the
206 circulating water to cool the assembly to near room temperature. Once the assembly cooled down,
207 the cooling water was shut off and the assembly was slowly depressurized.

208 Once a capsule was retrieved from the assembly, it was mounted in Petropoxy 154 and
209 stored in a furnace at 100 °C for 1 hour to harden. The mounted capsule was then grinded on a 600
210 grit SiC paper to expose material within the capsule. Once exposed, the sample was impregnated,
211 sometimes several times, with a low viscosity Petropoxy 154, i.e., freshly made, under vacuum to
212 limit the loss of material upon further polishing. The impregnated sample was then polished on a
213 nylon cloth with 3 micron diamond powder, followed by a 1 micron nylon cloth and/or a velvet
214 cloth using 0.3 micron alumina suspension liquid.

215

216 **2.3 Analysis of Run Products**

217

218 The polished samples were imaged and analyzed using a field emission gun electron microprobe

219 (JEOL JXA-8530F Hyperprobe) at the Department of Earth, Environmental and Planetary
220 Sciences at Rice University. Phases were identified using backscattered electron imaging, energy
221 dispersive X-ray spectroscopy (EDS), and compositionally analyzed using wavelength dispersive
222 X-ray spectroscopy (WDS). All phases were analyzed using 15 kV accelerating voltage. Olivine,
223 orthopyroxene, clinopyroxene, garnet, and amphibole were analyzed using fully focused electron
224 beam of 20 nA current. If a mineral phase showed compositional zoning from core to rim, spots
225 were chosen along the rims of those phases as such analytical volumes are expected to be closer
226 to equilibrium, in chemical communication with the adjacent phases. In order to obtain reliable
227 estimates of melt compositions from heterogeneously quenched melt pools, a defocused beam of
228 10 nA with spot sizes ranging from 10 to 50 microns was used. Analyses were taken across the
229 whole quench pool to assure that the data collected were not biased towards specific heterogeneous
230 regions. Most quench pools were analyzed on 2-3 sections by polishing off the old surface. The
231 analytical standards used for silicates were jadeite (Na), chrome diopside (Si, Ca, Mg), biotite (K),
232 olivine (Mg, Si, Fe), rutile (Ti), almandine (Si, Al), plagioclase (Si, Ca, Al), and rhodonite (Mn)
233 while the glasses were analyzed using a basaltic glass standard NMNH-113716-1.

234
235
236
237
238

239 **3. RESULTS**

240
241

242 The experimental conditions, phase assemblages, and available phase proportions are given in
243 Table 2 and the back scattered electron images of experimental products are shown in Figure 2. A
244 phase diagram, constructed for our bulk composition DP + 10% MM is shown in Figure 3.

245
246

247 3.1. Textures and Phase Assemblages

248

249 Experiments performed at 2 GPa, 900-1000 °C contain olivine, orthopyroxene, and amphibole and
250 are texturally similar to experiments at 3 GPa in this temperature interval in that most
251 orthopyroxene exists as fine grained laths often surrounding euhedral amphiboles (Figure 2D,
252 Supplementary Figure 1). The experiment conducted at 2 GPa, 1050 °C (Run B458) contains
253 silicate melt along olivine and orthopyroxene grain boundaries where the silicate melt is bounded
by round bubble walls, interpreted to indicate the presence of a fluid phase (Figure. 2B).

254 Experiments at >1050 °C reached melt fractions large enough to segregate into melt pools
255 composed of heterogeneously dispersed quenched silicate glass and metastable quenched phases
256 (Figures. 2C & 2F). The quench texture of the hydrous silicate melts in our experiments resemble
257 those in previous hydrous partial melting experiments (Green, 1973, Till et al., 2012, Mallik et al.,
258 2015).

259 The experiment at 3 GPa, 950 °C (run number B444) is dominated by euhedral olivine, and
260 fibrous orthopyroxene, clinopyroxene, garnet, and amphibole surrounded by fine grain laths of
261 orthopyroxene (Supplementary Figure 1). Experiments at 3 GPa, 900-1000 °C are all interpreted
262 as subsolidus due to a lack of quenched melt and the relative homogeneous distributions of
263 minerals throughout the capsules. All subsolidus experiments at 3 GPa show identical mineralogy,
264 with exception to one small grain of rutile observed at 900 °C (which could be a disequilibrium
265 phase), and similar phase proportions and textures. These experiments are dominated by euhedral
266 olivine grains and fine grained fibrous orthopyroxene with minor amounts of amphibole,
267 clinopyroxene, and garnet (>10 wt.% collectively). Amphibole and clinopyroxene are often
268 enclosed within laths of residual orthopyroxene and are rarely in contact with olivine (Figure. 2D).
269 Mass balance, assuming 2 wt.% water in amphibole, suggests that most of the water in the system
270 (~96%) exists as a free fluid and therefore our experiments are aqueous fluid saturated below the
271 solidus. The consistent underestimation of Na in mineral phases relative to the bulk composition
272 suggests that the free fluid is rich in sodium, a highly soluble element in aqueous fluids at high P -
273 T conditions (Manning, 2004, Hermann and Spandler, 2008). Experiments at 3 GPa and >1000 °C
274 show a stark change in mineralogy and texture with the disappearance of amphibole, a change in
275 orthopyroxene texture from fine grain laths to euhedral crystals and a gradient in mineralogy across
276 the capsule similar to the experiment at the same temperature at 2 GPa. Clinopyroxene, garnet,
277 and orthopyroxene are concentrated towards the cold end of the capsule while the hot end is
278 dominated by olivine and fine wisps of quenched fluid/melt (Figure. 2F). The gradient in
279 mineralogy has been observed in previous water saturated peridotite experiments and is attributed
280 to the thermal compaction effect facilitated by the presence of melt in a small thermal gradient
281 (Lesher and Walker, 1988, Grove et al., 2006, Till et al., 2012, Mallik et al., 2015). The quench
282 pool at 3 GPa, 1050 °C (run B450) shows two distinct quench products, spherules and fine wisps
283 (Figure. 2F), interpreted as a quenched fluid containing dissolved solutes and a silicate melt,
284 respectively. Previous studies have interpreted the existence of these two distinct quench products

285 as evidence for the coexistence of a fluid and silicate melt below the second critical endpoint of
286 the peridotite + H₂O system (Mibe et al., 2007, Till et al., 2012).

287 The experiments using the DP + 5% MM mix (B474 & B488) produced similar phase
288 assemblages as the DP + 10% MM experiments (B459 & B473) at the same *P-T* conditions in that
289 they all are dominated by olivine and orthopyroxene with small modal abundances of
290 clinopyroxene and melt. However, the former experiments contained lower melt fractions relative
291 to the latter at a given *P-T* condition.

292 In general, the experiments ≤ 1000 °C at 2 and 3 GPa, contain 7-10 wt.% amphibole, and a
293 lack of evidence for quenched melt and mineralogical gradients. In experiments > 1000 °C at 2
294 and 3 GPa, amphibole disappears, quenched melt appears, and the experiments shows a gradient
295 in mineralogy from the hot to cold end of the capsule. These textural observations and phase
296 identifications place the solidus of our bulk composition at 1000 – 1050 °C at 2 and 3 GPa, which
297 is discussed in detail in a subsequent section.

298

299 **3.2. Approach to Equilibrium**

300

301 Reversal experiments were not performed in this study. However, the following criteria
302 can be used to establish maintenance of a closed system and a close approach to equilibrium: (a)
303 The low sum of squared residuals for all oxides in the subsolidus experiments ranged from 0.4 to
304 0.6 ensuring a closed system, with most deficiency coming from Na likely reflecting leaching into
305 an H₂O-rich fluid phase. Experiments with a melt present show larger sum of squared residuals,
306 between 0.6-1.5 with most of the deficiency coming from Fe due to exchange and loss to the
307 experimental capsule, (b) Long experimental durations ranging from 96 to 169 hours, which is
308 comparable to previous studies using volatile bearing peridotite compositions under similar *P-T*
309 conditions where approach to equilibrium was demonstrated (e.g., Mandler and Grove, 2016, Saha
310 et al., 2018, 2019). (c) Measured experimental temperatures and those calculated using the Brey
311 and Kohler (1990) thermometer vary by only 11-117 °C, given average phase compositions from
312 each experiment are used rather than adjacent rims, the monitored and estimated equilibrium
313 temperatures are considered quite similar (Table 2). (d) Small compositional heterogeneity within
314 each phase as evident from the small standard deviation among multiple WDS analyses for each
315 mineral, although minor zoning of olivine was observed in low temperature runs. (e) Kd_{Melt}^{OL} (Fe-

316 $Mg = 0.3 \pm .05$ (Table 3) for all melt bearing experiments is in perfect agreement with the
317 knowledge of this exchange coefficient (Roeder and Emslie, 1970, Kushiro and Mysen, 2002,
318 Filiberto and Dasgupta, 2011).

319

320 **3.3. Melt Compositions, Quench Modification, and Fe loss**

321

322 Melt compositions obtained using electron microprobe analyses are reported on an
323 anhydrous basis in Table 3 and plotted as a function of temperature in Figure 4. Experiments B458
324 and B474 (2 GPa - 1050 °C and 1100 °C) contain silica poor metastable quench crystals, which
325 were crystallized from the equilibrium melt upon quenching and depressurization of the
326 experiment (Fig. 2D). Because the quench crystals have different compositions than the coexisting
327 quenched silicate glass patches, analysis of the silicate glass alone will give erroneous melt
328 compositions often enriched in SiO_2 . Therefore, it is important to add these quenched phases back
329 into analyzed melt to avoid the misinterpretation of SiO_2 -rich melts in equilibrium with peridotite
330 minerals (Green, 1973, 1976). In Table 3, the estimated melt compositions of B458 and B474 are
331 calculated by adding quench amphibole and cpx, respectively, to the composition of the measured
332 glass until $Kd_{Melt}^{Ol} = 0.3$. It should be noted that even when adding quenched phases back to the
333 melt, they remain rich in SiO_2 and would be classified as dacites based on SiO_2 ($SiO_2 > 62$ wt.%).
334 Metastable quench phases are also observed in higher temperature experiments as constituents of
335 the large silicate melt pools (Figure 2C). In these experiments, we were able to integrate both
336 silicate glass and quench phases using defocused beam analyses with spot sizes of 10-50 microns
337 evenly across the whole melt pool, ensuring that the analyses encompassed both metastable quench
338 phases and altered residual silicate glass.

339 Fe loss to metal capsules are reported for each experiment in Table 2. Most experiments
340 suffered minimal Fe loss (<15 %), with exception to B486 which suffered 50% Fe loss to the
341 $Au_{75}Pd_{25}$ capsule. Fe was added back into the melt of B486 using the methods described in Mallik
342 et al., (2015) (see their supplementary information), although this method is only likely to provide
343 a guide for the FeO content of the melt composition and is unlike to yield accurate estimate (e.g.,
344 Mitchell and Grove, 2016).

345 In experiments at 2 GPa, with increasing temperature, SiO_2 decreases from 67 to 51.7 wt.%,
346 producing a wide spectrum of dacitic to basaltic compositions from 1050 to 1250 °C. TiO_2
347 increases from 0.3 to 0.5 wt. % from 1050 to 1100 °C, then plateaus around 0.5 wt.% until 1250

348 °C where it drops to around 0.3 wt.%. Al_2O_3 decreases from 26 to 6.7 wt.% and CaO increases
349 from 1.0 to 10.0 wt.% from 1050 to 1100 °C, then decreases from 10 to 5 wt.% from 1100 to 1250
350 °C. MgO and FeO increase from 0.8 and 0.6 wt.% to 22 and 10 wt.%, respectively. Na_2O increases
351 from 1.6 to 3.4 wt.% between 1050 and 1100 °C, then plateaus out at 3-3.5 wt.% up to 1250 °C.
352 K_2O , with the complete breakdown of amphibole, decreases from 2.3 to 0.4 wt.% from 1050 to
353 1250 °C.

354 In experiments at 3 GPa, with increasing temperature, SiO_2 decreases from 59 to 50 wt.%,
355 producing a spectrum of andesitic to basaltic compositions from 1050 to 1250 °C. TiO_2 decreases
356 from 0.9 to 0.3 wt.% from 1050 to 1250 °C. Al_2O_3 decreases from 19 to 6 wt.%, while CaO , in the
357 presence of cpx, increases from 2 to 9 wt.% from 1050 to 1150 °C, then decreases from 9 to 7
358 wt.% from 1150-1250 °C, i.e., in the absence of cpx. MgO and FeO increase from 6.7 and 3.9
359 wt.% to 24 and 9 wt.%, respectively with increasing degree of isobaric melting and increase in
360 temperature. Na_2O decreases from 3.7 to 2 wt.%, while K_2O decreases from 3.3 to 0.5 wt.% due
361 to the exhaustion of amphibole. Due to poorly preserved melt pool surfaces resulting in low probe
362 totals, H_2O content in the melt could not be reliably determined by difference in probe totals.
363 However, in experiments where an aqueous fluid was not present, H_2O contents were estimated
364 by mass balance, assuming all H_2O in experiments is dissolved in silicate melts. These estimates
365 are presented in Table 3.

366 The fluid saturated melt in the DP + 5% MM experiment at 2 GPa 1100 °C (B474) is richer
367 in SiO_2 and Al_2O_3 , and poorer in FeO , MgO , and CaO relative to the fluid saturated melt in the
368 DP + 10% MM experiment at the same P - T condition. In contrast, the fluid under-saturated melt
369 in the DP + 5% MM experiment at 3 GPa 1200 °C (B488) is within error similar to the fluid under-
370 saturated melt in the DP + 10% MM experiment at the same P - T condition in most oxides. Thus
371 the melt:rock ratio mostly affects compositions of low temperature, fluid-saturated melts.

372

373 **3.4. Compositions of residual minerals**

374

375 All mineral compositions are reported in Supplementary tables 1-5.

376 Olivine at 2 and 3 GPa is forsteritic with Mg# ~91 at 900 °C. Mg # steadily increases with
377 temperature to ~92.5, where olivine is in equilibrium with high degree melts (Supplementary Table
378 1).

379 Orthopyroxene compositions are enstatitic with Mg# >92. At 2 and 3 GPa, experiments at 900-
380 1050 °C contain orthopyroxenes with >1 wt.% Al₂O₃, with the lowest temperature orthopyroxenes
381 at 2 GPa containing 2.6 wt.% Al₂O₃. From 1050 to 1250 °C, Al₂O₃ in orthopyroxene drops to >0.5
382 wt.% (Supplementary Table 2).

383 Amphibole at 2 and 3 GPa is pargasitic with ~47-49 wt.% SiO₂, 20 wt.% MgO, 9-12 wt.%
384 Al₂O₃, 8.5-10.5 wt.% CaO, 0.8-1.5 wt% TiO₂, and 3-4 wt.% Na₂O + K₂O (Supplementary Table
385 3). Amphibole at 3 GPa is richer in Al₂O₃ and alkalis and poorer in SiO₂ and CaO compared to
386 amphiboles at 2 GPa. Alkali content in amphibole increases with increasing temperature from 3.1
387 to 4 and 4 to 4.18 wt.% at 2 and 3 GPa, respectively.

388 Clinopyroxene is diopside-rich in all experiments and have Mg# ~93. They contain ~ 17-
389 21 wt.% MgO and 20-21.5 wt.% CaO (Supplementary Table 4). At 3 GPa, clinopyroxenes are
390 richer in Al₂O₃ (~2.7 wt.%) and Na₂O (~1.2 wt.%) compared to clinopyroxenes at 2 GPa, and Na₂O
391 decreases from 1.3 to 0.78 wt.% as temperature increases from 900 to 1050 °C.

392 Garnets at 3 GPa are pyrope-rich (~65-75%), with variable proportion of almandine (~15-
393 17%) and grossular (13-17%) where the percentages are based on atoms per formula unit based on
394 12 oxygens. Mg# steadily increases from 79.4 to 82.5 with increasing temperature from 900 to
395 1050 °C (Supplementary Table 5).

398 4. DISCUSSION

400 4.1. The inferred solidus location

402 A change in texture and mineral distribution occurs in experiments >1000 °C at 2 and 3
403 GPa, corresponding to the first appearance of quenched melt. At low temperatures, i.e., ≤1000 °C,
404 experiments contain small subhedral olivine grains with diameters of 10-30 microns and fine
405 grained fibrous laths of opx often engulfing amphibole and cpx grains (Figure 2D, Supplementary
406 Figure 1). Similar fibrous textures are reported in other water saturated peridotite studies at
407 subsolidus conditions and likely represent crystal growth in the presence of water rich fluid (Mallik
408 et al., 2015, Pirard and Hermann, 2015). Low temperature experiments also lack mineralogical
409 gradients across the capsule (Figure. 2A) similar to inferred sub-solidus experiments of previous
410 water-rich fluid saturated peridotite studies (Grove et al., 2006, Till et al., 2012, Mallik et al.,

411 2015). These authors attribute the lack of mineralogical gradients to the presence of solely a fluid
412 phase in which silicate solubilities are too low to facilitate dissolution and reprecipitation of
413 minerals according to the thermal gradient of the capsule. These two textural criteria suggest that
414 the fluid phase in experiments ≤ 1000 °C is solely a water-rich fluid; therefore, we interpret these
415 experiments as subsolidus. The experiments at 1050 °C contain larger euhedral grains of olivine
416 and opx with diameters of 50-100 microns, lack the fibrous textures observed in sub-solidus
417 experiments, exhibit mineralogical gradients across the capsule, and are the lowest temperature
418 experiments in which silicate melts are clearly preserved (Figs. 2B , & 2F). These observations
419 suggest that the solidus of our metasomatized depleted peridotite is located at 1000 – 1050 °C at 2
420 and 3 GPa, in good agreement with many previous water saturated peridotite studies (Green, 1973,
421 Millhollen et al., 1974, Kawamoto and Holloway, 1997, Green et al., 2010, 2014) and distinctly
422 hotter than the fluid saturated solidus estimated in some studies (e.g., Mysen and Boettcher, 1975,
423 Grove et al., 2006, Till et al., 2012).

424 It is noted that the experiment at 2 GPa, 1000 °C contains a gradient in porosity across the
425 capsule (Fig. 2B), which previous authors have attributed to thermal compaction effect facilitated
426 by the presence of silicate melt in a small thermal gradient (Grove et al., 2006, Till et al., 2012).
427 However, because this experiment lacks cpx and garnet, the associated mineralogical gradient that
428 would accompany the thermal compaction effect is not observed. Therefore, it is not clear whether
429 the gradient in porosity is due to the presence of silicate melt or to random mineral pluck outs
430 during polishing. Although we place the solidus at 1000 -1050 °C at 2 GPa, we acknowledge the
431 possibility that silicate melt could have been present but not preserved in the experiment at 1000
432 °C. Whether the true solidus at 2 GPa is at 950 – 1000 °C or 1000 -1050 °C is not essential to this
433 study and evidence of the coexistence of silicate melt and a free fluid phase at 2 GPa, 1050 °C
434 (Fig. 2D) suggest that these conditions are very close to the true solidus given the relatively low
435 H₂O contents of the starting mix and the high solubility of H₂O in silicate melts at this pressure.
436 Again, even if the true solidus for our experiments is ~50 °C lower than what we infer, it would
437 still be distinctly higher than the low fluid-saturated solidus temperature places in some studies
438 (e.g., Mysen and Boettcher, 1975, Grove et al., 2006, Till et al., 2012). It is interesting to note,
439 however, that the lowest temperature experiment of Grove and Till (2019) where melt is clearly
440 observed in the BSE images is at 950 °C, yet these authors interpreted the solidus at 3 GPa to be
441 at 800-820 °C (Fig. 5) based on the mineralogical and textural arguments of Till et al. (2012).

442 Figure 5 shows the location of fluid saturated solidi from this study and previous
443 experimental studies on water saturated peridotite. The location of the water saturated fertile
444 peridotite solidus at 2-4 GPa from literature varies widely and has been a subject of debate most
445 notably between the studies of Grove et al. (2006), Till et al. (2012), and Green et al. (2010, 2014).
446 The inferred solidus of our depleted peridotite fluxed with a hydrous MORB-derived silicate melt
447 is similar to the higher temperature fluid-saturated solidus location, i.e., those determined in the
448 studies of Millhollen et al. (1974) and Green et al. (2010, 2014). The solidus of this study falls in
449 between the solidi inferred from Pirard and Hermann (2015) and Mallik et al. (2015) who studied
450 the interaction between hydrous sediment melt and olivine and fertile peridotite, respectively
451 (Figure. 5). Pirard and Hermann (2015) attributed their relatively low solidus temperatures to high
452 total alkali contents (2.1 wt.%) of their starting composition, which is considerably higher than our
453 starting composition (0.72 wt.%). This coupled with the extremely low CaO/Al₂O₃ (0.09) of their
454 starting composition, which lowers the upper stability limit of amphibole, likely leads to the highly
455 depressed solidus at 2-4 GPa (Mysen and Boettcher, 1974a). The starting composition used in
456 Mallik et al. (2015) also has high alkali contents (2.59 wt. %); however, the high Al₂O₃ and CaO
457 contents of the fertile peridotite component together with the highly alkaline and Al₂O₃ rich
458 sediment melt allowed for the stabilization of large modal abundances (>30 wt.%) of hydrous
459 minerals. The stabilization of amphibole and phlogopite makes H₂O and alkalis much more
460 compatible in the solid residue, which suppresses the effect of H₂O and alkalis on depressing the
461 peridotite solidus. This interpretation is similar to that posited by the work of Saha and Dasgupta
462 (2019), which argued on the control of K₂O/H₂O ratio on the fluid-saturated phase relations of
463 peridotite and on the stability of hydrous mineral such as phlogopite. This effect delays the onset
464 of major melting to the higher temperature dehydration solidus where the exhaustion of amphibole
465 releases mineral bound H₂O and alkalis (Mallik et al., 2015). In comparison, our relatively depleted
466 bulk composition stabilized low modal abundances amphibole (7-10 wt.%), and as a consequence
467 H₂O and alkalis are less compatible in the solid residue allowing for the onset of major melting to
468 occur at lower temperatures (Fig. 5). The same argument can be used to explain why Till et al.
469 (2012) do not observe amphibole, while we do. Till et al. (2012) used a starting composition with
470 an alkali/H₂O of 0.02 (14.5 wt% bulk H₂O) compared to our bulk composition with alkali/H₂O
471 ratio of 0.2 (3.5 wt% bulk H₂O). It is not surprising, therefore, that the experiments of Till et al.
472 (2012) lacked and ours yielded amphibole. At low alkali/H₂O ratios, alkalis in the system are

473 preferentially dissolved in the excess free fluid, limiting their role in the stabilization of amphibole
474 (e.g., Saha and Dasgupta, 2019).

475

476 **4.2. Melting Reactions of Hydrous Peridotite**

477

478 The mass fractions of minerals and melts calculated by mass balance are presented in Table
479 2. These are used to calculate coefficients for melting reactions using the methods from Kinzler
480 (1997). At 2 and 3 GPa, the experiments at 950 and 1000 °C (B455 and B446), respectively, are
481 interpreted as subsolidus and are thus assumed to have melt modes at $F=0$. Textural evidence to
482 support this assumption is discussed in section 4.1. Using the calculated melt and mineral modes
483 from experiments at 950 °C and 1050 °C at 2 GPa, and experiments at 1000 °C and 1050 °C at 3
484 GPa, the melting reactions describing the production of the first melts at 2 and 3 GPa are as follows.

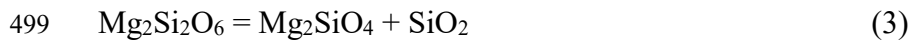
485 *Depleted Peridotite + MORB-derived Melt 2 GPa, 950 – 1050 °C (F = 0-6.6 wt.%)*



487 *Depleted Peridotite + MORB-derived Melt 3 GPa, 1000 – 1050 °C (F = 0-4.5 wt.%)*



489 The melting reactions are fluid-present, peritectic at both pressures as opx and amphibole
490 incongruently melt to form melt, olivine, and cpx, with minor amounts of garnet produced at 3
491 GPa. Equations 1 and 2 show that amphibole, the main storage site for CaO and Al₂O₃ in our
492 system at subsolidus conditions, is the dominant phase contributing to the melt forming reaction.
493 Aside from olivine, cpx is the dominant solid phase produced in the melt forming reaction, while
494 garnet is completely absent at 2 GPa, and produced in small quantities at 3 GPa. These reactions
495 show that CaO is compatible and Al₂O₃ is incompatible during the initiation of melting and can
496 explain the low CaO/Al₂O₃ observed in the partial melts at the onset of melting. Equations 1 and
497 2 also show that opx is consumed producing olivine + melt. Considering that SiO₂ in the melt is
498 strongly influenced by the following reaction:



500 (Orthopyroxene) (Olivine) (Melt)

501 the appearance of olivine on the melt side of reactions 1 and 2 offers an explanation as to why
502 near solidus melts at 2 and 3 GPa are silica-rich

503 Below, equations 4 and 5 are the near solidus melting reactions from the metasomatized
504 peridotite studies of Grove and Till (2019) and Pirard and Hermann (2015), respectively,

505 calculated from their published phase proportions. The bulk compositions of these studies are
506 listed in Table 1.

507 *Fertile Peridotite + H₂O + Alkalies 3.2 GPa (F= 5.1-7.5 wt.%)*

508 0.54 opx + 0.17 cpx + 0.13 garnet = 0.88 olivine + 1 melt (4)

509 *Olivine + Sediment-derived Hydrous Melt 2.5 GPa (F=0 – 15 wt.%)*

510 0.20 opx + 0.13 amph + 0.80 phlogopite = 0.13 olivine + 1 melt (5)

511 Similar to the near solidus melting reactions observed in our study, reactions 4 and 5 are
512 also peritectic in nature, generating olivine + SiO₂-rich melts. Therefore, it appears that when
513 hydrous peridotites of varying composition undergo low degree, fluid-saturated melting, opx is
514 consumed to produce olivine and silica-rich melts. However, if the system attains relatively high
515 bulk alkali/H₂O ratio, which takes place if the agent of water addition is hydrous slab-derived melt
516 or alkali-rich aqueous fluid, amphibole is involved in the peritectic, silica-rich melt-forming
517 reactions.

518 At higher degrees of melting, the phase contributing to melting changes at 2 and 3 GPa.
519 Using our modal proportions of experiments at 1100 °C and 1250 °C at 2 GPa, and at 1150 °C and
520 1250 °C at 3 GPa, the following melting reactions are calculated.

521 *2 GPa, 1100 – 1250 °C (F = 10-18.9 wt.%)*

522 1.8 olivine = 1 melt + 0.8 opx (6)

523 *3 GPa, 1150 – 1250 °C (F = 11.6-20.4 wt.%)*

524 1.9 olivine = 1 melt + 0.9 opx (7)

525 Between ~10 and 20 % melting, melt is in equilibrium with a harzburgite residue. Olivine
526 is consumed in the melting reactions producing melt + opx. Thus, at higher degrees of melting,
527 opx is produced in the melting reaction alongside SiO₂-poor melts (SiO₂ ~50 wt.%, Fig. 7).

528 Below is the high degree melting reaction from Grove and Till (2019)

529 *Fertile Peridotite + H₂O + Alkalies at 3.2 GPa (F=11.5 – 25 wt.%)*

530 0.09 olivine + 0.49 cpx + 0.64 garnet = 0.13 opx + 1 melt (8)

531

532 Equations 4 and 8 show that, similar to our study, the peritectic mineral, or the mineral
533 produced with melt, shifts from olivine to opx as melting degree increases in fertile peridotite
534 fluxed with a slab-derived melt. Thus, the shift from olivine to opx as the peritectic mineral as
535 melting degree increases is expected to take place in hydrous, metasomatised peridotites of varying
536 fertility at 2 – 3.2 GPa. The differences in fertility do, however, affect the stability of CaO- and

537 Al₂O₃-rich phases throughout the melting interval. In a fertile peridotite fluxed with hydrous
538 silicate melts, CaO and Al₂O₃ are compatible in cpx and garnet, respectivley, which contribute to
539 melting from $F = 5$ to 25 wt.%, and dominate the melting reactions at $F = 11.5\text{--}25$ wt.%. In a
540 depleted peridotite fluxed with hydrous MORB-derived melt, CaO and Al₂O₃ is mostly stored in
541 amphibole, which contributes to the melting reaction at $F = 0\text{--}6.6$ wt.%, after which olivine
542 dominates the melting reactions at $F = 10\text{--}20.4$ wt.%.

543

544 **4.3. Melt compositions and melting systematics of this study versus previous peridotite**
545 **melting studies with similar bulk H₂O**

546

547 In Figure 6, the melt compositions generated in this study as a function of the degree of
548 partial melting and pressure are compared to partial melts from peridotite + hydrous sediment melt
549 studies (Pirard and Hermann, 2015, Mallik et al., 2016), peridotite + H₂O studies enriched in
550 alkalis representing a metasomatic slab component (Mitchell and Grove, 2015, Grove and Till,
551 2019), and peridotite + H₂O study without an added slab component (Tenner et al., 2012). The
552 experiments chosen for comparison have bulk H₂O of 2.5-4.21 wt.%, similar to our DP + 10%
553 MM starting composition (3.5 wt.% H₂O). It has been shown that increasing H₂O in otherwise
554 similar starting composition leads to increased melt production and generates more quartz
555 normative melts at low pressures (Kushiro et al., 1968, Tenner et al., 2012, Mitchell and Grove
556 2015, Mallik et al., 2016), therefore, compiling experiments with similar bulk H₂O allows for
557 direct comparison of how melt compositions and melting systematics differ according only to
558 differences in pressure and major oxide compositions (Table 4).

559 Melts in this study are silica rich (>52 wt.% SiO₂) at ≤ 15 % melting and become incrisingly
560 more silica poor at higher degrees of melting, consistant with melts from the studies of Pirard and
561 Hermann (2015) and Grove and Till (2019) at 2-3.5 GPa. In general, at any given degree of partial
562 melting, SiO₂ increases with decreasing pressure (Figure 6). The experiments of Mitchell and
563 Grove (2015) show that silica rich melts can be generated to up to 30 wt.% melting at 1 GPa,
564 whereas at similar degrees of melting, experiments ≥ 3 GPa are silica poor (<48 wt.% SiO₂). The
565 effects of pressure, H₂O saturation and temperature on the SiO₂ concentration of partial melts can
566 explain the trends observed in the data. Mallik et al. (2016) showed that for a given melt H₂O
567 concentration, the activity coefficient of SiO₂ in melt (γ_{SiO_2}) is larger at higher pressures,

568 enhancing orthopyroxene over olivine formation and thus generating more silica deficient melts.
569 This explains the trend of decreasing SiO_2 with increasing pressure at a given melt fraction and
570 bulk H_2O content. Mallik et al. (2016) also showed that γ_{SiO_2} is near ideal ($\gamma_{\text{SiO}_2} \sim 1$) in melts
571 coexisting with a fluid phase, therefore, fluid saturated melts experience less prominent increase
572 in γ_{SiO_2} at high pressures. Furthermore, because the partitioning of FeO^* and MgO into the melt
573 is highly temperature dependent, low temperature melts near the depressed hydrous peridotite
574 solidus are poor in FeO^* and MgO , and are therefore rich in SiO_2 on an anhydrous basis (Gaetani
575 and Grove, 1998). These two considerations explain why near solidus H_2O saturated melts (<15
576 wt.% melting) in this study, Pirard and Hermann (2015), and Grove and Till (2019) are silica-rich
577 on an anhydrous basis (>57 wt.% SiO_2) even at high pressures (2-3 GPa). Given the diversity in
578 peridotite fertility (depleted vs. fertile) and metasomatic agent (e.g., MORB-derived melt vs.
579 sediment-derived melt or aqueous fluid) between this study, Pirard and Hermann (2015), and
580 Grove and Till (2019) (Table 4), it appears that the generation of silica rich, fluid-saturated melts
581 would occur over a range of metasomatized peridotite compositions with bulk H_2O around 3.5-4
582 wt.% in the mantle wedge up to 3.2 GPa.

583 TiO_2 is highly incompatible in this study and others plotted in Figure 6 and thus the starting
584 composition controls the melt TiO_2 content at a given degree of melting. Table 1 shows that the
585 bulk compositions of this study and Pirard and Hermann (2015) are poorer in TiO_2 relative to the
586 bulk composition of Grove and Till (2019). Therefore, our melts are poorer in TiO_2 than those
587 from Grove and Till (2019).

588 Al_2O_3 is highly incompatible in this study as amphibole, the dominant Al_2O_3 bearing phase
589 at 2 and 3 GPa, is completely exhausted in the melting reaction, forming the first melts (Equations
590 1 and 2). At <10 wt.% melting, our melts are more aluminous compared to those in Grove and Till
591 (2019), where near solidus experiments are saturated with 10 wt.% garnet, making Al_2O_3 more
592 compatible in the solid residue. As melting degree increases, Al_2O_3 in this study quickly drops due
593 to the lack of aluminous phases contributing to melting at 2 and 3 GPa (Equations 6 and 7, Figure.
594 6). At 10-20 wt.% melting, the melts in Grove and Till (2019) and Pirard and Hermann (2015) are
595 greater in Al_2O_3 compared to this study due to the continuous contribution of garnet and phlogopite
596 to the melting reactions, respectively (equations 4 and 5).

597 In our study, CaO is mildly compatible from 5-10 wt.% melting in the presence of residual
598 cpx and then becomes incompatible from 10-20 wt.% melting at 2 and 3 GPa. From 10-20 wt.%

599 melting and in the absence of cpx, CaO decreases as olivine dominates the melting reaction
600 (Equations 6 and 7). At < 20 wt.% melting, CaO in the melts from Grove and Till (2019) and
601 Pirard and Hermann (2015) are poorer compared to those in this study due to the compatibility of
602 CaO in cpx and very low CaO in the starting composition, which controls cpx mass fraction,
603 respectively (Table 4). Cpx is completley exhausted at ~20 wt.% melting in the fertile peridotite
604 compositions (bulk CaO >2.5 wt.%) of Grove and Till (2019), Mallik et al. (2016), Mitchell and
605 Grove (2015), and Tenner et al.(2012). Phases that are chief repository of CaO are exhausted at
606 lower melt fractions in our depleted peridotite experiments relative to fertile peridotite
607 experiments, causing the switch from compatible to incompatible behaviour of CaO to occur at
608 higher melt fractions in fertile peridotites.

609 FeO* and MgO behave compatibly in our study due to the predominance of olivine and
610 opx as residual phases at all pressures and temperatures (Table 2). At < 10 % melting, our melts
611 along with melts of Grove and Till (2019) and Pirard and Hermann (2015) are FeO* and MgO
612 poor due to the low temperatures of these experiments ≤ 1050 °C and the strong dependence of
613 FeO* and MgO partitioning on temperature (Gaetani and Grove, 1998). At 10-20 wt.% melting in
614 this study, olivine becomes the only phase contributing to the melting reactions at 2 and 3 GPa,
615 causing a rapid increase in FeO* and MgO with increasing melting degree (Equations 6 and 7). In
616 contrast, the melting reactions from Grove and Till (2019) are dominated by cpx and as a
617 consequence their melts are poorer in FeO* and MgO relative to ours in this melting interval
618 (Equation 8). One striking feature of this data compilation is the variation in FeO* and MgO with
619 pressure at 20-30% melting. At a given melt fraction, the 3.5 GPa experimental melts of Tenner et
620 al. (2012) are much richer in FeO* and MgO relative to the 1 GPa experiment of Mitchell and
621 Grove (2015). Because these two studies were performed at similar temperature intervals (1250-
622 1350 °C), this trend is not due to the sensitivity of FeO* and MgO partitioning on temperature but
623 instead is a reflection of the tendency of melts to be more olivine normative at higher pressures at
624 a given melt fraction (Mitchell and Grove, 2015).

625 Na₂O and K₂O in our study behaves incompletely from 5-20 wt.% melting at 2 and 3 GPa
626 due to disappearance of amphibole near the solidus and the subsequent lack of alkali bearing
627 phases contributing to melting reactions from 10 – 20 wt.% melting at 2 and 3 GPa (Equations 6
628 and 7). The fluid saturated melt at 2 GPa (5 wt.% melting) is poorer in Na₂O than what is expected
629 for an incompatible element at low melt fractions likely due to the high solubility of Na₂O in the

630 coexisting fluid phase as noted by Green et al. (2010). Also, it is likely that some Na₂O was lost
631 during EPMA analysis by Na migration in the glass. The melts from Pirard and Hermann (2015)
632 and Mallik et al. (2016) are richer in K₂O at a given melt fraction when compared to this study.
633 These studies used sediment-derived melt as a fluxing agent, which is more K₂O-rich relative to
634 MORB-derived melts such as the one used in this study (Figure. 1), making their bulk
635 compositions much richer in K₂O relative to this study (Table 1).

636

637

638 **4.4. Effect of H₂O, Peridotite Fertility, and Pressure on Melt SiO₂ Contents and Melt 639 Productivity of Mantle Wedge**

640 Compared to lavas produced at mid ocean ridges, primitive arc lavas and associated plutons
641 with Mg# > 50 vary widely in SiO₂, ranging from basalts (45 – 52 wt. % SiO₂) to high magnesium
642 andesites and basaltic andesites (52 – 62 wt. % SiO₂) (Kelemen et al., 2003). In order to evaluate
643 the cause for such compositional diversity observed in primitive arc magmas, in Figure 7 we plot
644 the SiO₂ concentrations on an anhydrous basis of partial melts derived from this study and various
645 other hydrous peridotite melting studies conducted over a range of bulk H₂O, pressure and
646 temperatures applicable to mantle wedges. Changing these three variables produces melts, which
647 range from 42 to 68 wt. % SiO₂, covering and exceeding the compositional range with respect to
648 SiO₂ observed in primitive arc lavas. Figure 7 is divided into three segments, experiments
649 preformed at 1-1.6, 2-2.5, and 3-3.5 GPa, corresponding to melting in the shallow mantle wedge
650 near the moho, the hot core of the mantle wedge, and the base of the mantle wedge near the
651 slab/wedge interface, respectively. Below we discuss the effects of H₂O, pressure, temperature,
652 and peridotite fertility on the melt productivity and SiO₂ concentration of primitive hydrous
653 mantle-derived melts.

654

655 *4.4.1. Effect of Peridotite Fertility on Isobaric Melt Productivity*

656 While H₂O is the dominant factor leading to variations in melting degree at a given pressure
657 and temperature, the isobaric melt productivity (IMP) differs significantly between the hydrous
658 depleted peridotite compositions in this study and Pirard and Hermann (2015) compared to more
659 fertile compositions used in Grove and Till (2019). At 2 and 3 GPa, our IMP is 5.8 and 7.9 wt.%
660 melt/ 100 °C from 1050 – 1250 °C, similar to the IMP of the depleted peridotite from Pirard and

661 Hermann (2015) (8 wt.% melt/ 100 °C). In contrast, the IMP of hydrous fertile peridotites from
662 Grove and Till (2019) is 23.0 and 27.0 wt.% melt/ 100 °C, about 3 times greater than the IMP
663 calculated for hydrous depleted peridotites at 2 and 3 GPa. As a consequence, the melting degree
664 at a given temperature is much higher in fertile peridotite compositions relative to our depleted
665 peridotite composition (Figure 7D).

666 The contrast in IMP between hydrous fertile and depleted peridotites is likely due to
667 depleted peridotite residues being dominated by olivine (Table 2) as opposed to more fusible
668 minerals such as opx, cpx, garnet, and phlogopite, which are present in large proportions in the
669 fertile peridotite residues in Mallik et al. (2015 and 2016) and Grove and Till (2019).

670

671

672 *4.4.2. Effect of Bulk H₂O on Melting Degree and SiO₂ Concentration*

673 From Figure 7, it is apparent that the bulk H₂O exerts a strong control on the degree of
674 partial melting, where bulk compositions with higher H₂O have a higher degree of partial melting
675 at a given temperature. Mallik et al. (2016) showed that the melting degree of fertile peridotite is
676 largely independent of the fluxing agent (slab-derived hydrous melts vs. pure H₂O), and that bulk
677 H₂O content is the main variable leading to differences in melting degree at a given temperature.
678 Figure 7 confirms this effect of bulk H₂O on melting degree from 1 to 3.5 GPa and shows that bulk
679 H₂O is the dominant variable controlling melting degree throughout the whole mantle wedge.

680 At 1-1.6 GPa, corresponding to the shallow mantle wedge, SiO₂ concentrations in H₂O
681 undersaturated melts (black borders) are positively correlated with bulk H₂O (Figure 7A).
682 Therefore, at a given temperature, bulk compositions with higher H₂O generate SiO₂-rich basaltic
683 andesites from 1100-1300 °C (Mitchell and Grove, 2015), whereas studies with low bulk H₂O
684 produce SiO₂-poor basalts in this temperature interval (Hirose and Kawamoto, 1995). The most
685 silica rich melts produced at 1-1.6 GPa are fluid saturated and are andesitic, the melting degree of
686 which can vary widely depending on the bulk H₂O of the starting material (Figure 7B). Because
687 higher bulk H₂O leads to higher degrees of melting at a given temperature, the production of melts
688 that are sufficiently low degree to be fluid saturated and hence andesitic is restricted to low
689 temperatures <1100 °C in the shallow mantle wedge regardless of bulk H₂O.

690 At 2-2.5 GPa, SiO₂ decreases with increasing temperature and melt fraction in this study
691 and Pirard and Herman (2015), both producing fluid saturated andesitic to dacitic melts (Figure

692 7C). However, the experiments from Pirard and Hermann (2015) produced andesitic melts at 900-
693 1000 °C, corresponding to near the slab-wedge interface, and about 100 °C cooler than the
694 conditions of andesite production in our experiments. Thus, differences in bulk composition, which
695 have control on the location of the fluid saturated solidus, will affect how far above the slab/wedge
696 interface the first low degree andesitic to dacitic melts will form. It is also clear that differences in
697 melt/rock ratio affect the melting degree and SiO₂ contents of fluid saturated melts at a given
698 temperature. At 1100 °C, the degree of melting in our DP + 5% MM experiment with 1.7 wt. %
699 H₂O is lower compared to that in our DP + 10% MM experiment with 3.5 wt.% H₂O and
700 consequently is more SiO₂ rich. Thus a depleted peridotite fluxed with 5 wt.% MORB-derived
701 hydrous silicate melt produces more SiO₂ rich melts compared to a depleted peridotite fluxed with
702 10 wt.% of the same melt at a given temperature during fluid saturated melting. Fluid
703 undersaturated melts also decrease in SiO₂ with increasing temperature and melt fraction until
704 around 1200 °C where SiO₂ contents plateau to around 50 wt.%, similar to those in Mallik et al.
705 (2015, 2016).

706 At 3-3.5 GPa, SiO₂ steadily decreases at temperatures <1150 °C in this study, Grove and
707 Till (2019), and Pirard and Herman (2015) (Figure. 7E). Similar to melting at lower pressure, fluid
708 saturated melts at 3-3.5 GPa are the most SiO₂-rich and their formation is restricted to low
709 temperatures <1100 °C. Fluid saturated andesitic melts are first produced at 1050 °C in this study,
710 whereas similar melts from Grove and Till (2019) are produced as low as 925 °C. Therefore, it
711 appears that fertile peridotite will produce H₂O saturated andesitic melts closer to the slab/wedge
712 interface compared to our depleted peridotite when fluxed with a hydrous slab melt. At
713 temperatures >1200 °C SiO₂ increases with increasing temperature and degree of melting in this
714 study, as well as in the studies of Mallik et al. (2015 and 2016) and Tenner et al. (2012). Mallik et
715 al. (2016) showed that at high pressures, SiO₂ in melt increases with decreasing dissolved H₂O in
716 fluid-undersaturated melts. Therefore, for a given bulk H₂O, higher degree melting leads to
717 dilution of H₂O and hence higher SiO₂ in the melt. A minimum melt SiO₂ at high pressures is then
718 defined by the lowest degree and hence most H₂O-rich fluid-undersaturated melt corresponding to
719 1100 -1200 °C in Figure. 7E. At temperatures below this this minimum, melts are fluid saturated
720 and therefore SiO₂ rich, and at temperatures above this minimum fluid-undersaturated melts become
721 diluted in H₂O as melting degree increases and hence melts become SiO₂ rich. It should be noted
722 that the negative correlation between dissolved H₂O and SiO₂ in fluid under-saturated melts is

723 distinct for high pressure (> 2 GPa) mantle melting (Mallik et al., 2016), whereas at low pressures,
724 more dissolved H₂O in the melt leads to enrichments in SiO₂ (Gaetani and Grove, 1998, Mitchell
725 and Grove, 2015).

726

727

728 *4.4.3. Effect of Pressure on melt SiO₂ concentration*

729 Figure 7 shows that fluid-undersaturated melts (black borders) are more SiO₂ poor at a given
730 temperature at higher pressures. Fluid-undersaturated melts generated at 1150 -1300 °C at 1 GPa
731 are basaltic andesites with SiO₂ of 52 – 57 wt.%. Within this same temperature interval, melts at 2
732 GPa range from basaltic andesites to basalts with SiO₂ of 54 -48 wt.% and melts at 3 GPa are
733 basalts and SiO₂ poor picro-basalts with SiO₂ of 50 – 42 wt.%. Therefore, if melting in the mantle
734 wedge occurs under fluid-undersaturated conditions, melts are expected to be more SiO₂ rich the
735 further above the slab/wedge interface they are generated. Pressure does not appear to have a strong
736 effect on SiO₂ concentrations of fluid-saturated melts where at 1 and 3 GPa, melts are both
737 andesitic with SiO₂ around 60 wt.% at 1000 – 1100 °C. However, our data show that at 2 GPa,
738 H₂O saturated melts produced at 1000 – 1100 °C are dacitic and significantly more SiO₂ rich than
739 H₂O saturated andesitic melts at 3 - 3.2 GPa from this study and Grove and Till (2019). If SiO₂ in
740 fluid-saturated melts does increase at lower pressures, the similarity in melt SiO₂ contents between
741 fluid saturated melts at 1 and 3 GPa may be due to differences in bulk composition between this
742 study and those in Figure 7A which may offset the effect of pressure.

743

744 **4.5. Comparison between Experimental Partial Melts and Primitive Arc Magmas**

745

746 Substantial H₂O contents in primitive arc basalts, typically around 3-4 wt.%, (Anderson
747 1974, Sisson and Grove 1993b, Sobolev and Chaussidon 1996, Plank et al., 2013), and primitive
748 arc andesites, >4.5 wt.% (Grove et al., 2003), offers evidence for the crucial role of slab derived-
749 H₂O in flux melting of the mantle wedge and is interpreted as the dominant mechanism for the
750 production of calc-alkaline arc (Zimmer et al., 2010). However, the exact nature of the slab-derived
751 fluxing agent, whether it be hydrous silicate melts derived from subducting basaltic crust (This
752 Study), sediments (Pirard and Herman, 2015, Mallik et al., 2015 and 2016) or an H₂O-dominated
753 fluid with some dissolved elements such as alkalis (Mitchell and Grove, 2015, Grove and Till,

754 2019), is poorly known due to the inability to directly observe processes occurring at the
755 slab/wedge interface. Therefore, comparison of experimental melts generated over a wide range
756 of pressures, temperatures, and compositions with primitive arc lavas can offer insights into not
757 only the physical conditions necessary to produce specific primary arc lavas, but also the nature of
758 the slab-derived fluxing agent.

759

760 *4.5.1. Filtering and Correcting Natural Data*

761 Most arc lavas erupted at the surface have undergone significant fractional crystallization
762 since last equilibration with the mantle, therefore a direct comparison cannot be made between the
763 output at volcanic arcs with high Mg# experimental melts in equilibrium with mantle minerals. To
764 overcome this issue, global arc lava compositional data attained using the PetDB database were
765 filtered for primitive samples with $MgO \geq 6$ wt. % and then corrected for fractional crystallization
766 by the addition of olivine until equilibration with Fo_{92} was achieved ($Mg\# \sim 77$). Fo_{92} was chosen
767 as the equilibrium olivine composition in accordance with the average olivine composition of our
768 experiments (Supplementary table 1). This gave 676 corrected whole rock arc lava data
769 represented as small gray circles and plotted on an anhydrous basis in Figure 8. Also plotted are
770 primitive andesites and basaltic andesites taken from Mitchell and Grove (2015), which have $Mg\# > 70$,
771 $SiO_2 \geq 51$ wt.% and $MgO \geq 7$ wt.%. These data collectively show the vast compositional
772 diversity among primitive arc lavas ranging from andesites to picro-basalts. Below, we discuss
773 how differences in pressure and H_2O content during hydrous mantle melting can account for the
774 chemical diversity observed in arc lavas.

775

776 *4.5.2. General Trends in Natural and Experimental Data*

777 Figure 8 shows that the MgO , FeO^* , and CaO contents of primitive arc magmas are
778 negatively correlated with SiO_2 whereas Al_2O_3 and Na_2O are positively correlated. There is no
779 clear trend between K_2O and SiO_2 , but it is important to note the majority of primitive arc magmas
780 have $K_2O < 2$ wt.%.

781 The experimental data show similar compositional trends and overlap with the majority of
782 primitive arc magmas. There is a clear negative trend between pressure and SiO_2 contents of fluid
783 undersaturated melts. 1 GPa melts are mostly basaltic andesites, 2 GPa melts are basalts and
784 basaltic andesites, 3 GPa melts are basalts, and 3.5 GPa melts comprise the most SiO_2 poor picro-

785 basalts (Figure 8). Interestingly, all oxides among experimental melts vary with SiO_2 in near
786 identical ways as natural primitive arc magmas. Therefore, to first order, differences solely in
787 pressure from 1 to 3.5 GPa are adequate to explain the trend and spread in natural primitive arc
788 magmas globally. The exception to this is that fluid saturated melts are SiO_2 rich at all pressures
789 from 1 to 3.5 GPa. When extrapolating the experimental results onto the natural data, it appears
790 that fluid saturated melting at 1 – 3 GPa (Figures 7 and 8), produces rare primitive andesites with
791 $\text{SiO}_2 > 57$ wt.%, where H_2O undersaturated melting produces more common basaltic andesites,
792 basalts, and picrobasalts at 1, 2-3, and 3.5 GPa, respectively.

793

794 4.5.3. *Conditions of Primitive Arc Magma Genesis*

795 Natural picro-basalts have the highest FeO^* and MgO contents and lowest SiO_2 , Al_2O_3 ,
796 CaO , and Na_2O contents. Partial melting experiments of hydrous garnet peridotite at 3.5 GPa from
797 Tenner et al. (2012) reproduce natural picro-basalts in SiO_2 , MgO , Al_2O_3 , Na_2O , and K_2O , but are
798 more FeO^* -poor and CaO -rich. The discrepancy in FeO^* between the melts in Tenner et al., (2012)
799 and natural picro-basalts may be due to Fe loss to the metal capsule, which was not corrected even
800 though up to 30% Fe-loss was reported. Our most silica poor melt, located in the picro-basalt field
801 in Figure 8, is much more alkali-rich than natural arc picro-basalts and would be classified as a
802 basanite in a TAS diagram and based on the classification of Le Bas (1989). Because alkalis are
803 highly incompatible, the alkali-rich nature of this melt is likely due to it being the lowest degree,
804 fluid undersaturated melt in our study.

805 Basalts, ranging from 45 to 52 wt.% SiO_2 , are the most common primitive arc magmas.
806 Thus, the conditions of arc basalt genesis should translate to the most prevailing conditions of
807 mantle wedge melting. Our fluid-undersaturated melts at 3 GPa match well with primitive arc
808 basalts in all oxides presented in Figure 8, with the exception of MgO and Al_2O_3 contents. At 1200
809 – 1250 °C, our hydrous partial melts are richer in MgO and poorer in Al_2O_3 by about 5 wt.%
810 relative to the majority of primitive arc basalts. However, because these experimental melts are in
811 equilibrium with $\text{Fo}_{93.95}$, this discrepancy in MgO can in part be explained by natural arc basalts
812 being corrected to equilibration with Fo_{92} . Peridotite + hydrous sediment-derived melt experiments
813 at 2-3 GPa match primitive arc basalts in most oxides, but are far richer in K_2O compared to the
814 majority of primitive arc basalts. This implies that during the production of arc basalts and hence
815 the majority of primitive arc magmas in active subduction zones, either K-rich sediment-derived

816 melts are unlikely fluxing agents, or that fluxing of the mantle wedge with continental sediment-
817 derived melts occurs at much lower melt:rock ratios (<0.25) than those explored in the studies of
818 Pirard and Herman (2015) and Mallik et al. (2015 and 2016). The 3.2 GPa experiments on
819 peridotite + H₂O + alkalis, which in many ways is the fertile analog of our alkali rich depleted
820 peridotite composition (Table 1), matches primitive arc basalts in all oxides presented in Figure 8.
821 Therefore, the production of arc basalts can be explained by fluid-undersaturated melting of
822 peridotites varying in fertility at 3 GPa so long as the bulk K₂O is relatively low (<1 wt.%).

823 Our fluid undersaturated melts at 2 GPa, along with peridotite + H₂O + alkalis experiments
824 at 1 GPa, match primitive basaltic andesites in all oxides. Our depleted peridotite melts are
825 generally richer in MgO and FeO* and poorer in Al₂O₃ and CaO relative to the fertile peridotite
826 melts at 1 GPa; however, the spread in melts produced between both endmembers cover the range
827 of natural basaltic andesites. This implies that differences in mantle composition can account for
828 the oxide variability of partial melts at a given SiO₂ content. In this sense, the trends in primitive
829 arc magma compositions are on first order controlled by pressure, and on second order controlled
830 by bulk composition of metasomatised mantle source.

831 Lastly, it is clear that silica-rich melts are produced by fluid saturated melting of peridotites
832 from 1 – 3.5 GPa. Dacitic melts produced at 2 GPa lie far from primitive arc magma compositions
833 suggesting that low degree melts rarely escape the mantle wedge unaltered. The andesitic melt
834 produced at 2 GPa in this study is richer in CaO and closer in composition to primitive andesites
835 than andesitic melts produced at 3 GPa in this study and Grove and Till (2019). Because of the
836 wide range of pressures and mantle compositions in which andesites are generated experimentally,
837 one would expect for their appearance to be commonplace. However, as Figure 8 shows, primitive
838 andesites are rare among arc lavas globally. Two possible explanations for the rarity of primitive
839 andesites is that

- 840 1. Fluid-saturated melting is uncommon in the mantle wedge due to high temperatures and
841 high degrees of partial melting. If this is the case, then primary andesite production in the
842 mantle wedge is a rare process.
- 843 2. Andesitic melts are predominately formed at the base of the mantle wedge near the
844 slab/wedge interface where temperatures are low enough to produce near solidus, fluid-
845 saturated melts. These hydrous melts then rise buoyantly and react with higher temperature
846 peridotites in the core of the mantle wedge generating more common basalts and basaltic

847 andesites by higher degree, fluid-undersaturated melting.

848

849

850

851 **5. CONCLUDING REMARKS**

852

853 We performed high *P-T* experiments investigating the melting behavior of a depleted
854 peridotite metasomatized by a MORB-derived hydrous silicate melt in variable proportion and its
855 relation to subduction zone magmatism. Between 0 and 5 % melting, amphibole and opx
856 dominate the melting reactions, generating fluid-saturated melts which are SiO₂- and Al₂O₃-rich
857 and FeO*- and MgO-poor primitive andesites. These low degree melting reactions are
858 incongruent, consuming opx and producing olivine + SiO₂-rich melts, a behavior which is
859 observed over a wide range of starting compositions and pressures. As melting degree increases,
860 a spectrum of basaltic andesites to basanites are produced under fluid-undersaturated conditions.

861 Comparing our experimental melts and experimental melts from other hydrous peridotite
862 melting studies with natural primitive arc magmas, it is clear that melting of peridotites with
863 varying bulk compositions but with 2.5 – 4.2 wt. % H₂O can reproduce the major oxide spread
864 and trends of primitive arc magmas globally. Differences solely in pressure during fluid-
865 undersaturated melting can account for the first order compositional trends of primitive arc
866 magmas ranging from basaltic andesites to picrumbasalts and basanites, where differences in
867 temperature and bulk composition are second order controls that account for the spread of major
868 oxides at a given SiO₂ content.

869 In comparison with ultrapotassic melts generated in the peridotite + hydrous sediment-
870 derived melt experiments, our experiments match better with natural primitive arc magmas in
871 most oxides and in particular K₂O. Because ultrapotassic arc magmas are rare among arcs
872 globally, K₂O-rich fluxing agents such as sediment-derived melts are unlikely fluxing agents in
873 the mantle wedge. Instead, K₂O-poor hydrous melts derived from subducted MORB are more
874 likely fluxing agents in the mantle wedge.

875 Finally, the ubiquity of andesite genesis during fluid-saturated melting over a wide range
876 of pressures and peridotite starting compositions suggests that rarity of primitive andesites in
877 volcanic arcs is related to the fact fluid-saturated melting is restricted to the distal portion of the
878 wedge melting environment, i.e., at the base of the mantle wedge where temperatures are
879 relatively low. These fluid-saturated andesitic melts then likely react with the hotter overlying

880 peridotite to produce higher degree fluid-undersaturated basalts and basaltic andesites.

882 **ACKNOWLEDGMENTS**

884 We gratefully acknowledge thoughtful, critical reviews by Tom Sisson, Etienne Medard, and Gene
885 Yodzinski, which helped us improve the communication. This research was funded by NSF
886 grant EAR-1763226 to R.D.

888 **REFERENCES**

889 Anderson A. T. (1974) Evidence for a Picritic, Volatile-rich Magma beneath Mt. Shasta, California. *Jour. Petrol.* **15**,
890 243-267.

891 Arai S., Takada S. and Michibayashi K., et al. (2004) Petrology of Peridotite Xenoliths from Iraya Volcano,
892 Philippines, and its Implication for Dynamic Mantle-Wedge Processes. *Jour. Petrol.* **45**, 369-389.

893 Brey G. P. and Kohler T. (1990) Geothermobarometry in Four-phase Lherzolites II. New Thermobarometers, and
894 Practical Assessment of Existing Thermobarometers. *Jour. Petrol* **31**, 1353-1378.

895 Cai Y., LaGatta A. and Goldstein G. L., et al. (2014) Hafnium isotope evidence for slab melt contributions in the
896 Central Mexican Volcanic Belt and implications for slab melting in hot and cold slab arcs. *Chem. Geol.* **377**,
897 45-55.

898 Conceiçao R. V. and Green D. H. (2004) Derivation of potassic (shoshonitic) magmas by decompression melting of
899 phlogopite+pargasite lherzolite. *Lithos* **72**, 209-229.

900 Cooper L. B., Plank T. and Wallace P. J., et al. (2012) Global variations in H₂O/Ce: 1. Slab surface temperatures
901 beneath volcanic arcs. *Geochem. Geophys. Geosyst.* **13**, 3.

902 Defant M. J. and Drummond M. S. (1990) Derivation of some modern arc magmas by melting of young subducted
903 lithosphere. *Nature* **347**, 662-665.

904 Drummond M. S., Defant M. J. and Kepezhinskas P. K. (1996) Petrogenesis of slab-derived trondhjemite-tonalite–
905 dacite/adakite magmas. *Earth Environ Sci Trans R Soc Edinb.* **87**, 205-215.

906 Drummond M. S and Defant M. J. (1990) A Model For Trondhjemite-Tonalite-Dacite Genesis and Crustal Growth
907 via Slab melting: Archean to Modern Comparisons. *J. Geophys. Res.* **95**, 21503

908 Ertan I. E. and Leeman W. P. (1996) Metasomatism of Cascades subarc mantle: Evidence from a rare phlogopite
909 orthopyroxenite xenolith. *Geology* **24**, 451.

910 Filiberto J. and Dasgupta R. (2011) Fe²⁺-Mg partitioning between olivine and basaltic melts: Applications to genesis
911 of olivine-phyric shergottites and conditions of melting in the Martian interior. *Earth Planet. Sci. Lett.* **304**,
912 527-537.

913 Fumagalli P., Zanchetta S. and Poli S. (2009) Alkali in phlogopite and amphibole and their effects on phase relations
914 in metasomatized peridotites: a high-pressure study. *Contrib. Mineral. Petrol.* **158**, 723-737.

915 Gaetani G. A. and Grove T.L. (1998) The influence of water on melting of mantle peridotite." *Contrib. Mineral.*
916 *Petrol.* **131**, 323-346
917 Gill J.B. (1981) Orogenic Andesites and Plate Tectonics. *Springer, Berlin.* **390**
918 Green D. H. (1976) Experimental Testing of "Equilibrium" Partial Melting of Peridotite Under Water-Saturated, High-
919 Pressure Conditions *Can. Mineral.* **14**, 255-268
920 Green D. H. (1973) Experimental melting studies on a model upper mantle composition at high pressure under water-
921 saturated and water-undersaturated conditions. *Earth Planet. Sci. Lett.* **19**, 37-53.
922 Green D. H., Rosenthal A. and Kovács I. (2012) Comment on "The beginnings of hydrous mantle wedge melting",
923 CB Till, TL Grove, AC Withers, Contributions to Mineralogy and Petrology, DOI 10.1007/s00410-011-
924 0692-6. *Contrib. Mineral. Petrol* **164**, 1077-1081.
925 Green D. H., Hibberson W. O. and Rosenthal A., et al. (2014) Experimental Study of the Influence of Water on
926 Melting and Phase Assemblages in the Upper Mantle. *Jour. Petrol.* **55**, 2067-2096.
927 Green D. H., Rosenthal A. and Kovacs I., et al. (2010) Water and its influence on the lithosphere–asthenosphere
928 boundary. *Nature* **467**, 448-451.
929 Grove T. L. and Till C. B. (2019) H₂O-rich mantle melting near the slab–wedge interface. *Contrib. Mineral. Petrol*
930 **174**, 80.
931 Grove T. L., Elkins-Tanton L. T. and Parman S. W., et al. (2003) Fractional crystallization and mantle-melting controls
932 on calc-alkaline differentiation trends. *Contrib. Mineral. Petrol* **145**, 515-533.
933 Grove T. L., Chatterjee N. and Parman S. W., et al. (2006) The influence of H₂O on mantle wedge melting. *Earth*
934 *Planet. Sci. Lett.* **249**, 74-89.
935 Hacker B. R. (2008) H₂O subduction beyond arcs. *Geochem. Geophys. Geosyst.* **9**, Q03001.
936 Halama R., Savov I. P. and Rudnick R. L., et al. (2009) Insights into Li and Li isotope cycling and sub-arc
937 metasomatism from veined mantle xenoliths, Kamchatka. *Contrib. Mineral. Petrol.* **158**, 197-222.
938 Hermann J. and Spandler C. J. (2008) Sediment Melts at Sub-arc Depths: an Experimental Study. *Jour. Petrol.* **49**,
939 717-740.
940 Hermann J. and Green D. H. (2001) Experimental constraints on high pressure melting in subducted crust. *Earth*
941 *Planet. Sci. Lett.* **188**, 149-168.
942 Hermann J., Spandler C. and Hack A., et al. (2006) Aqueous fluids and hydrous melts in high-pressure and ultra-high
943 pressure rocks: Implications for element transfer in subduction zones. *Lithos* **92**, 399-417.
944 Hirose K. and Kawamoto T. Hydrous partial melting of lherzolite at 1 GPa: The effect of H₂O on the genesis of
945 basaltic magmas." *Earth Planet. Sci. Lett.* **133**, 463-473.
946 Hirose K. (1997) Melting experiments on lherzolite KLB-1 under hydrous conditions and generation of high-
947 magnesian andesitic melts. *Geology* **25**, 42.
948 Hirschmann M. M. (2000) Mantle solidus: Experimental constraints and the effects of peridotite composition.
949 *Geochem. Geophys. Geosyst.* **1.10**, 2000GC000070
950 Ishimaru S., Arai S. and Ishida Y., et al. (2006) Melting and Multi-stage Metasomatism in the Mantle Wedge beneath

951 a Frontal Arc Inferred from Highly Depleted Peridotite Xenoliths from the Avacha Volcano, Southern
952 Kamchatka. *Jour. Petrol.* **48**, 395-433.

953 Kamenov G. D., Perfit M. R. and Mueller P. A., et al. (2008) Controls on magmatism in an island arc environment:
954 study of lavas and sub-arc xenoliths from the Tabar–Lihir–Tanga–Feni island chain, Papua New Guinea.
955 *Contrib. Mineral. Petrol.* **155**, 635-656.

956 Kawamoto T. and Holloway J. R. (1997) Melting Temperature and Partial Melt Chemistry of H₂O-Saturated Mantle
957 Peridotite to 11 Gigapascals. *Science*. **276**, 240-3.

958 Kay R. W. and. Mahlburg-Kay S. (1991) Creation and destruction of lower continental crust." *Geol. Rund.* **80**, 259-
959 278.

960 Kelemen P. B. (1995) Genesis of high Mg# andesites and the continental crust. *Contrib. Mineral. Petrol.* **120**, 1-19.

961 Kelemen, P. B., Yogodzinski G. M. and Scholl D. W. (2003) Along-strike variation in the Aleutian Island Arc:
962 Genesis of high Mg# andesite and implications for continental crust. *Geophys. Monogr. Ser.* **138**, 223-276.

963 Kepezhinskas P. K., Defant M. J. and Drummond M. S. (1995) Na Metasomatism in the Island-Arc Mantle by Slab
964 Melt—Peridotite Interaction: Evidence from Mantle Xenoliths in the North Kamchatka Arc. *Jour. Petrol.*
965 **36**, 1505-1527.

966 Kessel R., Ulmer P. and Pettke T., et al. (2005) The water–basalt system at 4 to 6 GPa: Phase relations and second
967 critical endpoint in a K-free eclogite at 700 to 1400 °C. *Earth Planet. Sci. Lett.* **237**, 873-892.

968 Kilian R. and Stern C. R. (2002) Constraints on the interaction between slab melts and the mantle wedge from adakitic
969 glass in peridotite xenoliths. *Eur. J. Mineral.* **14**, 25-36.

970 Kimura J., Gill J. B. and Kunikiyo T., et al. (2014) Diverse magmatic effects of subducting a hot slab in SW Japan:
971 Results from forward modeling. *Geochem. Geophys. Geosyst.* **15**, 691-739.

972 Kinzler R. J. (1997) Melting of mantle peridotite at pressures approaching the spinel to garnet transition: Application
973 to mid-ocean ridge basalt petrogenesis. *J. Geophys. Res. Solid Earth* **102**, 853-874.

974 Kushiro I. (1972) Effect of Water on the Composition of Magmas Formed at High Pressures. *Jour. Petrol.* **13**, 311-
975 334.

976 Kushiro I. and Mysen B. O. (2002) A possible effect of melt structure on the Mg-Fe²⁺ partitioning between olivine
977 and melt. *Geochim. Cosmochim. Ac.* **66**, 2267-2272.

978 Kushiro I., Syono Y. and Akimoto S. (1968) Melting of a peridotite nodule at high pressures and high water
979 pressures." *J. Geophys. Res.* **73**, 6023-6029.

980 Laurie A. and Stevens G. (2012) Water-present eclogite melting to produce Earth's early felsic crust. *Chem. Geol.*
981 **314-317**, 83-95.

982 Le Bas M. J. (1989) Nephelinitic and Basanitic Rocks. *Jour. Petrol.* **30**, 1299-1312

983 Lesher C. E. and Walker D. (1988) Cumulate Maturation and Melt Migration in a Temperature Gradient. *J. Geophys.*
984 *Res.* **93**, 10295-10311

985 Mallik A., Dasgupta R. and Tsuno K., et al. (2016) Effects of water, depth and temperature on partial melting of
986 mantle-wedge fluxed by hydrous sediment-melt in subduction zones. *Geochim. Cosmochim. Ac.* **195**, 226-

987 243.

988 Mallik A., Nelson J. and Dasgupta R. (2015) Partial melting of fertile peridotite fluxed by hydrous rhyolitic melt at
989 2–3 GPa: implications for mantle wedge hybridization by sediment melt and generation of ultrapotassic
990 magmas in convergent margins. *Contrib. Mineral. Petrol.* **169**, 48.

991 Mandler B. E. and Grove T. L. (2016) Controls on the stability and composition of amphibole in the Earth's mantle.
992 *Contrib. Mineral. Petrol.* **171**, 68.

993 Manning C.E. (2004) The chemistry of subduction-zone fluids. *Earth Planet. Sci. Lett.* **223**, 1-16.

994 Marschall H. R. and. Schumacher J. C. (2012) Arc magmas sourced from mélange diapirs in subduction zones *Nat.*
995 *Geosci.* **5**, 862-867.

996 Martin H. (1986) Effect of steeper Archean geothermal gradient on geochemistry of subduction-zone magmas. *Geol.*
997 **14**, 753.

998 Martin H. (1993) The mechanisms of petrogenesis of the Archaean continental crust—Comparison with modern
999 processes. *Lithos* **30**, 373-388.

1000 Maury R. C., M. J. and Joron J. (1992) Metasomatism of the sub-arc mantle inferred from trace elements in Philippine
1001 xenoliths. *Nature* **360.6405**, 661-663.

1002 McInnes I. A., Gregoire M. and Binns R. A., et al. (2001) Hydrous metasomatism of oceanic sub-arc mantle, Lihir,
1003 Papua New Guinea: petrology and geochemistry of fluid-metasomatised mantle wedge xenoliths. *Earth*
1004 *Planet. Sci. Lett.* **188**, 169-183.

1005 Médard E. and Grove T. L. (2006) Early hydrous melting and degassing of the Martian interior. *J. Geophys. Res.* **111**,
1006 11003.

1007 Mibe K., Kanzaki M. and Kawamoto T., et al. (2007) Second critical endpoint in the peridotite-H₂O system." *J.*
1008 *Geophys. Res.* **112.B3**, B03201.

1009 Mitchell A. L. and Grove T. L. (2015) Melting the hydrous, subarc mantle: the origin of primitive andesites. *Contrib.*
1010 *Mineral. Petrol.* **170**, 13

1011 Millholen G. L., Irving A. J., and Wyllie, P. J. (1974) Melting interval of peridotite with 5.7 per cent water to 30
1012 kilobars *J. Geol.* **82**, 575-587

1013 Morishita T., Dilek Y. and Shallo M., et al. (2011) Insight into the uppermost mantle section of a maturing arc: The
1014 Eastern Mirdita ophiolite, Albania. *Lithos* **124.3-4**, 215-226.

1015 Mysen B. O. and Boettcher A. L. (1975) Melting of a Hydrous Mantle: I. Phase Relations of Natural Peridotite at High
1016 Pressures and Temperatures with Controlled Activities of Water, Carbon Dioxide, and Hydrogen. *Jour.*
1017 *Petrol.* **16.1**, 520-548.

1018 Mysen B. O. and Boettcher A. L. (1975) Melting of a Hydrous Mantle: II. Geochemistry of Crystals and Liquids
1019 Formed by Anatexis of Mantle Peridotite at High Pressures and High Temperatures as a Function of
1020 Controlled Activities of Water, Hydrogen, and Carbon Dioxide." *Jour. Petrol.* **16.1**, 549-593.

1021 Niida K. and Green D. H. (1999) Stability and chemical composition of pargasitic amphibole in MORB pyrolite under
1022 upper mantle conditions. *Contrib. Mineral. Petrol.* **135.1**, 18-40.

1023 Pirard C. and Hermann J. (2015) Focused fluid transfer through the mantle above subduction zones. *Geol.* **43.10**, 915-
1024 918.

1025 Pirard C. and Hermann J. (2015) Experimentally determined stability of alkali amphibole in metasomatised dunite at
1026 sub-arc pressures." *Contrib. Mineral. Petrol.* **169.1**, 1.

1027 Pirard C., Hermann J. and O'Neill H. C. (2013) Petrology and Geochemistry of the Crust–Mantle Boundary in a
1028 Nascent Arc, Massif du Sud Ophiolite, New Caledonia, SW Pacific. *Jour. Petrol.* **54.9**, 1759-1792.

1029 Plank T., Kelley K. A. and Zimmer M. M., et al. Why do mafic arc magmas contain ~4wt% water on average? *Earth*
1030 *Planet. Sci. Lett.* **364**, 168-179.

1031 Plank T., Cooper L. B. and Manning C. E. (2009) Emerging geothermometers for estimating slab surface temperatures.
1032 *Nat. Geosci.* **2.9**, 611-615.

1033 Poli S. and Schmidt M. W. (2002) Petrology of Subducted Slabs. *Annu. Rev. Earth Planet. Sci.* **207**, 35

1034 Prouteau G., Scaillet B. and Pichavant M., et al. (1999) Fluid-present melting of ocean crust in subduction zones.
1035 *Geol.* **27.12**, 1111.

1036 Prouteau G., Scaillet B. and Pichavant M., et al. (2001) Evidence for mantle metasomatism by hydrous silicic melts
1037 derived from subducted oceanic crust. *Nature* **410**, 197-200.

1038 Rapp R. P., Shimizu N. and Norman M. D., et al. Reaction between slab-derived melts and peridotite in the mantle
1039 wedge: experimental constraints at 3.8 GPa. *Chem. Geo.* **160**, 335-356.

1040 Rapp R. P., Shimizu N. and Norman M. D. (2003) Growth of early continental crust by partial melting of eclogite.
1041 *Nature* **425**, 605-609.

1042 Rapp R. P., Watson B. E. and Miller C. F. (1991) Partial melting of amphibolite/eclogite and the origin of Archean
1043 trondhjemites and tonalites. *Precambrian Res.* **51**, 1-25.

1044 Roeder P. L. and Emslie R. F. (1970) Olivine-liquid equilibrium. *Contrib. Mineral. Petrol.* **29**, 275-289.

1045 Ryabchikov I. D., Miller C. and Mirwald P. W. (1996) Composition of hydrous melts in equilibrium with quartz
1046 eclogites. *Miner. Petro.* **58**, 101-110.

1047 Saha S. and Dasgupta R. (2019) Phase Relations of a Depleted Peridotite Fluxed by a CO₂-H₂O Fluid—Implications
1048 for the Stability of Partial Melts Versus Volatile-Bearing Mineral Phases in the Cratonic Mantle. *J. Geophys.*
1049 *Res. Solid Earth* **124**, 10089-10106.

1050 Saha S., Dasgupta R. and Tsuno K. (2018) High Pressure Phase Relations of a Depleted Peridotite Fluxed by CO₂-
1051 H₂O-Bearing Siliceous Melts and the Origin of Mid-Lithospheric Discontinuity. *Geochem. Geophys.*
1052 *Geosyst.* **19**, 595-620.

1053 Scambelluri M. and Philippot P. (2001) Deep fluids in subduction zones. *Lithos* **55**, 213-227.

1054 Schiano P., Clocchiatti R. and Shimizu N., et al. (1995) Hydrous, silica-rich melts in the sub-arc mantle and their
1055 relationship with erupted arc lavas. *Nature* **377**, 595-600.

1056 Schmidt M. W. and Poli S. (1998) Experimentally based water budgets for dehydrating slabs and consequences for
1057 arc magma generation. *Earth Planet. Sci. Lett.* **163**, 361-379.

1058 Sekine T. and Wyllie P. J. (1982) The System Granite-Peridotite-H₂O at 30 kbar, with Applications to Hybridization

1059 in Subduction Zone Magmatism. *Contrib. Mineral. Petrol.* **81**, 190-202

1060 Sen C. and Dunn T. (1994) Experimental modal metasomatism of a spinel Iherzolite and the production of amphibole-
1061 bearing peridotite. *Contrib. Mineral. Petrol.* **119**, 422-432

1062 Sisson T. W. and Kelemen P. B. (2018) Near-solidus melts of MORB + 4 wt% H₂O at 0.8–2.8 GPa applied to issues
1063 of subduction magmatism and continent formation. *Contrib. Mineral. Petrol.* **173**, 70.

1064 Sisson T. W. and Grove T. L. (1993) Temperatures and H₂O contents of low-MgO high-alumina basalts. *Contrib.*
1065 *Mineral. Petrol.* **113**, 167-184.

1066 Sobolev A. V. and Chaussidon M. (1996) H₂O concentrations in primary melts from supra-subduction zones and mid-
1067 ocean ridges: Implications for H₂O storage and recycling in the mantle. *Earth Planet. Sci. Lett.* **137**, 45-55.

1068 Spandler C. and Pirard C. (2013) Element recycling from subducting slabs to arc crust: A review. *Lithos* **170**, 208-
1069 223.

1070 Syracuse E. M., van Keken P. E. and Abers G. A. (2010) The global range of subduction zone thermal models. *Phys.*
1071 *Earth. Planet. In.* **183**, 73-90.

1072 Tatsumi Y., Hamilton D. L. and Nesbitt R. W. (1986) Chemical characteristics of fluid phase released from a
1073 subducted lithosphere and origin of arc magmas: Evidence from high-pressure experiments and natural
1074 rocks." *J. Volcanol. Geoth. Res.* **29**, 293-309.

1075 Tenner T. J., Hirschmann M. M. and Humayun M. (2012) The effect of H₂O on partial melting of garnet peridotite at
1076 3.5 Gpa *Geochem. Geophys. Geosyst.* **13**, 3016.

1077 Till C. B., Grove T. L. and Withers A. C. (2012) The beginnings of hydrous mantle wedge melting. *Contrib. Mineral.*
1078 *Petrol.* **163**, 669-688.

1079 Tsuno K. and Dasgupta R. (2011) Melting phase relation of nominally anhydrous, carbonated pelitic-eclogite at 2.5–
1080 3.0 GPa and deep cycling of sedimentary carbon. *Contrib. Mineral. Petrol.* **161**, 743-763.

1081 Ulmer P. (2001) Partial melting in the mantle wedge — the role of H₂O in the genesis of mantle-derived ‘arc-related’
1082 magmas. *Phys. Earth. Planet. In.* **127**, 215-232.

1083 van Keken P. E., Kiefer B. and Peacock S. M. (2002) High-resolution models of subduction zones: Implications for
1084 mineral dehydration reactions and the transport of water into the deep mantle. *Geochem. Geophys. Geosyst.*
1085 **3**, 1-20.

1086 van Keken P. E., Hacker B. R. and Syracuse E. M., et al. Subduction factory: 4. Depth-dependent flux of H₂O from
1087 subducting slabs worldwide. *J. Geophys. Res.* **116**, B01401.

1088 Walowski K. J., Wallace P. J. and Hauri E. H., et al. (2015) Slab melting beneath the Cascade Arc driven by
1089 dehydration of altered oceanic peridotite. *Nat. Geosci.* **8**, 404-408.

1090 Walowski K. J., Wallace P. J. and Clynné M. A., et al.. (2016) Slab melting and magma formation beneath the southern
1091 Cascade arc. *Earth Planet. Sci. Lett.* **446** (2016): 100-112.

1092 Yogodzinski G. M. and Kelemen P. B. (1998) Slab melting in the Aleutians: implications of an ion probe study of
1093 clinopyroxene in primitive adakite and basalt. *Earth Planet. Sci. Lett.* **158**, 53-65

1094 Yogodzinski G. M., Brown S. T. and Kelemen P. B., et al. (2015) The Role of Subducted Basalt in the Source of

1095 Island Arc Magmas: Evidence from Seafloor Lavas of the Western Aleutians. *Jour. Petrol.* **56**, 441-492.
1096 Zimmer M. M., Plank T. and Hauri E. H., et al. The Role of Water in Generating the Calc-Alkaline Trend: New
1097 Volatile Data for Aleutian Magmas and a New Tholeiitic Index. *Jour. Petrol.* **51**, 2411-2444
1098

1099
1100 **Figure 1.** Comparison of starting compositions used in with study with previous hydrous
1101 peridotite melting studies. Depleted peridotite composition plotted is that of AVX-1 from
1102 Kepezhinskas et al. (1995), also the depleted peridotite composition used in this study. MO is the
1103 MORB-derived hydrous silicate melt used in this study, RK89 from Kessel et al. (2005). DP +
1104 10% MM and DP + 5% DP are the two bulk compositions used in this study. Fertile peridotite is
1105 KLB-1 (Hirose 1997). Peridotite + SedM is taken from peridotite + hydrous sediment melt studies
1106 (Mallik et al., 2015, Pirard and Hermann 2015). Peridotite + MM is taken from peridotite +
1107 hydrous MORB melt studies (Sekine and Wyllie 1982, Prouteau et al., 2001). Peridotite + SM is
1108 from peridotite + slab melt studies where the slab melt was not specified as MORB or sediment-
1109 derived (Mitchell and Grove 2015, Grove and Till 2019). Peridotite + H₂O starting compositions
1110 from previous studies (Hirose 1997, Niida and Green 1999, Conceicoa and Green 2004, Fumagalli
1111 et al., 2009, Tenner et al., 2012). Sub arc mantle xenoliths are also from literature (Maury et al.,
1112 1992, McInnes et al., 2001, Kamenov et al., 2008, Halama et al., 2009). Gray oval is the range of
1113 sediment-derived melts generated at 2.5-4.5 GPa 800-1050 °C from Hermann and Spandler
1114 (2008). Sediment-derived melt compositions are plotted to compare against our MORB-derived
1115 melt composition. The MORB-derived melt used in this study is K₂O free and thus is not plotted
1116 in the MgO vs. K₂O plot. Notice the main difference between sediment and MORB-derived melt
1117 is the K₂O content, with the former being K₂O rich while the latter is K₂O-poor or K₂O-free. In
1118 addition, the MORB-derived hydrous melt is also poorer in alumina and richer in CaO.

1119
1120
1121
1122
1123
1124
1125
1126
1127
1128

1129
1130
1131
1132
1133
1134
1135
1136
1137 **Table 1** Composition of starting materials from this study and previous hydrous peridotite melting
1138 studies

Reference	This Study	This Study	This Study	This Study	Grove and Till (2019)	Mallik et al., (2015)	Pirard and Hermann (2015)	Mitchel and Grove (2015)	Mitchel and Grove (2015)	Tenner et al. (2012)
Starting Material	DP ^A	MM ^B	DP + 10 % MM ^C	DP + 5 % MM ^D	FP ^E + SM ^F	75% FP + 25% SedM ^G	75 % Ol 25% SedM	FP + SM	FP + SM	FP
SiO ₂	45.47	49.64	45.88	45.68	46.3	49.86	47.92	45.12	44.62	42.81
TiO ₂	0	0.6	0.06	0.03	0.18	0.21	0.09	0.18	0.17	0.12
Al ₂ O ₃	0.71	6.9	1.32	1.02	4.21	6.13	3.1	4.11	4.06	2.97
FeO*	7.59	1.57	6.99	7.29	7.48	6.14	6.64	7.28	7.21	8.28
MnO	0.12	0	0.11	0.12	0.1	0.1	0.11	0.1	0.1	0.09
MgO	44.82	1.12	40.45	42.64	37.18	28.58	35.81	36.17	35.83	39.93
CaO	0.93	1	0.94	0.93	3.2	2.44	0.28	3.11	3.08	2.87
Na ₂ O	0.32	4.03	0.69	0.5	0.59	0.98	1.29	0.59	0.57	0.19
K ₂ O	0.04	0	0.04	0.04	0.15	1.55	0.81	0.16	0.14	0.02
H ₂ O	0	35.14	3.51	1.76	4.21	4	3.96	3.19	4.21	2.5
Total	100	100	100	100	100.05	100	100	100	100	99.78

1139 ^A Depleted peridotite AVX-51 from Kepezhinskas et al. (1995) used as the base peridotite in this
1140 study. DP = Depleted Peridotite

1141 ^B MORB-derived hydrous silicate melt RK89 from Kessel et al. (2005) used as the metasomatic
1142 agent in this study. MM = MORB-derived melt

1143 ^C Bulk composition 1 used in this study is a homogenous mixture consisting of 90 wt.% DP and
1144 10 wt.% MM

1145 ^D Bulk composition 2 used in this study is a homogenous mixture consisting of 95 wt.% DP and 5
1146 wt.% MM

1147 ^E FP = fertile peridotite

1148 ^F SM = slab-derived melt not specified as sediment or MORB melt. Added as extra alkalis to an
1149 otherwise fertile peridotite.

1150 ^G SedM = subducted sediment-derive melt.

1151 * All Fe reported as FeO

Table 2. Summary of experimental conditions, phase assemblages, and available phase proportions

Exp. No	T (°C)	TBK	P (GPa)	Duration (h)	Capsule	Ol	Opx	Cpx	Grt	Amph	Melt	Σr^2	Aqueous Fluid	%Fe loss
90% DP + 10% MM														
B454	900	-	2	166	Au	53.0 (9)	39 (1)	-	-	7.6 (8)	-	0.6 (2)	3.4 (0)	-5.6
B455	950	-	2	120	Au	53 (1)	37 (1)	-	-	9.3 (3)	-	0.5 (4)	3.3 (0)	-4
B456	1000	-	2	142	Au	58.0 (5)	31.6 (7)	-	-	10.4 (3)	-	0.6 (1)	3.3 (0)	-7.3
B458	1050	1091	2	169	Au	57.0 (9)	34 (1)	2.6 (2)	-	-	6.2 (3)	1.4 (2)	+	-9.8
B459	1100	1100	2	145	Au	63.1 (9)	26.1 (9)	+	-	-	10.7 (5)	1.4 (2)	+	-12.5
B462	1150	-	2	146	Au	57.2 (7)	30 (1)	-	-	-	12.6 (5)	0.4 (0)	-	-4.4
B464	1200	-	2	141	Au ₇₅ Pd ₂₅	52 (1)	34 (1)	-	-	-	14.0 (3)	1.5 (3)	-	-14
B484	1250		2	97	Au ₇₅ Pd ₂₅	48 (1)	33 (2)	-	-	-	19 (1)	0.5 (1)	-	-4
B443*	900	1017	3	118	Au	52.6 (3)	37.6 (2)	1.3 (1)	+	8.5 (1)	-	0.3 (1)	3.4 (0)	-1.8
B444	950	975	3	142	Au	57.7 (5)	32.8 (4)	0.8 (0)	0.8 (0)	7.8 (2)	-	0.4 (1)	3.4 (0)	-4
B446	1000	1011	3	143	Au	52.0 (2)	40 (1)	0.6 (0)	0.1 (0)	7.7 (3)		0.5 (1)	3.4 (0)	-3.6
B450	1050	1130	3	141	Au	56.9 (7)	34.5 (6)	3.5 (1)	0.5 (0)	-	4.5 (1)	0.6 (2)	+	-2.6
B451	1100		3	96	Au	+	+	-	-	-	+	-	+	-
B453	1150	-	3	144	Au	58 (1)	30 (2)	-	-	-	12 (1)	0.7 (1)	-	-12
B473	1200	-	3	119	Au ₇₅ Pd ₂₅	50 (2)	34 (1)	-	-	-	16 (1)	0.5 (2)	-	-6.6
B486	1250		3	140	Au ₇₅ Pd ₂₅	42 (1)	38 (2)	-	-	-	20.4 (9)	0.8 (2)	-	-50
95% DP + 5% MM														
B474	1100		2	116	Au	69.7 (9)	23 (1)	1.6 (2)	-	-	5.5 (3)	0.4 (1)	+	-2
B488	1200		3	145	Au ₇₅ Pd ₂₅	61 (1)	32 (1)	0.2 (2)	-	-	7.3 (3)	0.8 (1)	-	-11

1152 The experiments are arranged, first for the DP + 10%MM and second for the DP + 5%MM bulk
1153 composition. For each composition, the experiments are arranged in the order of increasing
1154 pressure and at each pressure, in the order of increasing temperature. TBK – temperature estimated
1155 from two-pyroxene thermometer from Brey and Kohler (1990). Phase proportions estimated by
1156 mass balance calculations on an anhydrous basis. Numbers in parentheses are the $\pm 1\sigma$ determined
1157 by propagating errors in each oxide by Monte Carlo simulations (n = 10). For example, 53.0 (9)
1158 should be read as 53 ± 0.9 wt.% and 53.3 (1.0) as 53.3 ± 1.0 wt.%. ‘-’ indicates that phase was not
1159 present in the experiment. ‘+’ indicates that the phase was either present but in such low amounts
1160 that its proportion could not be estimated using mass balance, or in the case of B451, present but
1161 mass balance was not achieved due to a lack of glass analysis. Ol-olivine, Opx-orthopyroxene,
1162 Cpx-clinopyroxene, Gt-garnet, Amph-amphibole. Aqueous fluid was estimated by assuming 2
1163 wt.% water in amphibole and subtracting the amount of water contained in amphibole from the
1164 water content of the bulk composition (3.5 wt.%). This fluid phase is assumed to be pure water.
1165 *Exp. No 443 contained one small grain of rutile, which may be a disequilibrium phase, and is not
1166 incorporated into the table as an equilibrium phase.

1167 **Figure 2.** BSE images of experiments at 2 and 3 GPa, 950 – 1150 °C. (A) Highest temperature
1168 inferred subsolidus experiment at 2 GPa exhibiting fibrous opx and euhedral amphibole grains.
1169 The gradient in porosity might suggest the presence of silicate melt; however, due to a lack of
1170 observed quenched melt, this experiment is interpreted as subsolidus. (B) Magnified image of
1171 B458 showing silicate melt between olivine and orthopyroxene grain boundaries. Silicate melt is
1172 bounded by bubble walls, interpreted as evidence for the generation of silicate melt in the presence
1173 of an aqueous fluid phase. Silicate melt is composed of glassy patches along with quench phases
1174 (white needles), interpreted as quench products exsolved out of the equilibrium melt upon
1175 quenching the experiment. The quench products are similar to amphibole; however, their low Mg#
1176 ~ 84 suggests they are quench products as discussed in Pirard and Hermann (2015). (C) Fluid-
1177 undersaturated melt pool in B462 showing large segregated melt pool with heterogeneously spaced
1178 metastable quenched phases throughout. (D) Sub-solidus phase assemblage and texture showing
1179 euhedral amphibole and clinopyroxene surrounded by fine grained laths of fibrous orthopyroxene,
1180 garnet with poykilitic texture and euhedral olivine grains. (E) Experiment at 3 GPa showing
1181 mineralogical gradient across the capsule. Cpx (white phases) and gt (poykilitic light gray phases)
1182 are concentrated near and decreases away from the cold end of the capsule. (F) Magnified image
1183 of melt strands in B450 displaying evidence of quenched fluid (spherules) coexisting with a silicate
1184 melt, similar to those discussed in Till et al. (2012).

1185
1186 **Figure 3.** Phase diagram showing the stability of mineral and melt phases in the *P-T* space for our
1187 DP + 10% MM starting composition. Black dots are the *P-T* conditions of the experiments
1188 performed in this study. Olivine (Ol) and orthopyroxene (Opx) are present in all experiments.
1189 Other phases are Amph - pargasitic amphibole, Cpx, - clinopyroxene, Gt - garnet, Melt - silicate
1190 melt and fluid. At 2 GPa, cpx and gt are absent at inferred subsolidus conditions. At 3 GPa, minor
1191 amounts of cpx and gt (< 2 wt.% collectively) are present at inferred subsolidus conditions. Fluid-
1192 present, amphibole-out boundary marks the solidus, producing cpx and melt at 2 GPa and cpx, gt,
1193 and melt at 3 GPa. Garnet and cpx are exhausted at 1050 – 1100 °C at 3 GPa and cpx is exhausted
1194 at 1100 – 1150 °C at 2 GPa. Above 1150 °C at 2 and 3 GPa, melt is in equilibrium with a
1195 harzburgite residue (ol + opx). The two experiments using DP + 5% contained the same phase
1196 assemblages as the DP + 10% MM experiments in the phase diagram at the same *P-T* conditions,
1197 denoted by encircled data points.

Table 3. Partial melt compositions generated in this study.

Run no	B458	B458	B459	B462	B464	B484	B450	B453	B473	B486	B474	B474	B488
H ₂ O in bulk	3.51	3.51	3.51	3.51	3.51	3.51	3.51	3.51	3.51	3.51	1.75	1.75	1.75
Pressure (GPa)	2	2	2	2	2	2	3	3	3	3	2	2	3
Temperature (°C)	1050	1050	1100	1150	1200	1250	1050	1150	1200	1250	1100	1100	1200
Method	Measured	Estimated ^A	Measured	Fe Corr ^B	Measured	Estimated	Measured						
Melt %	6.20	5.03	10.74	12.58	14.02	18.86	4.50	11.60	15.65	20.42	4.18	5.50	7.27
SiO ₂	68 (1)	66.81	59 (2)	55 (1)	52 (2)	52 (1)	60.0 (9)	49 (3)	48 (1)	50 (3)	70 (1)	68.78	44 (2)
TiO ₂	0.2 (1)	0.38	0.45 (2)	0.42 (9)	0.37 (9)	0.3 (1)	0.88 (3)	0.50 (9)	0.37 (2)	0.28 (4)	0.6 (1)	0.59	0.36 (2)
Al ₂ O ₃	26 (1)	25.30	14.1 (8)	12 (1)	13 (1)	6.7 (7)	19 (1)	12 (4)	9.7 (3)	6 (2)	22.5 (5)	20.61	11.8 (5)
FeO	0.6 (1)	0.72	4.0 (4)	6.9 (6)	6.3 (3)	10.0 (7)	3.9 (3)	8 (1)	10.3 (4)	9 (2)	1.2 (4)	1.28	7.5 (9)
MnO	0.01(1)	0.01	0.05 (3)	0.07 (3)	0.03 (3)	0.16 (4)	0.04 (4)	0.13 (2)	0.06 (4)	0.07 (4)	0.17 (3)	0.18	0.5 (1)
MgO	0.8 (7)	1.35	7 (2)	15 (2)	13 (1)	22 (1)	6.7 (2)	16 (3)	24 (2)	24 (6)	0 (2)	2.28	19 (2)
CaO	1.0 (7)	1.64	9 (3)	7 (2)	10 (1)	5 (1)	2 (1)	9 (2)	5 (3)	7 (4)	2 (1)	3.69	9 (2)
Na ₂ O	1.6 (4)	1.59	3.4 (7)	3.2 (6)	3.3 (5)	3.0 (2)	3.7 (5)	2.8 (4)	1.8 (3)	2 (1)	1.8 (3)	1.66	5 (1)
K ₂ O	2.3 (2)	2.19	0.9 (1)	0.9 (1)	0.5 (2)	0.4 (1)	3.2 (2)	1.1 (5)	0.5 (2)	0.5 (4)	1.0 (1)	0.92	0.6 (1)
H ₂ O ^C	?	?	?	28 (2)	25 (1)	19 (4)	?	30 (4)	22 (5)	17 (3)	?	?	24 (1)
Mg#	73 (13)	77.00	76 (5)	80 (2)	79 (5)	79 (1)	75 (7)	78 (3)	79 (7)	83.00	42 (11)	76.00	82 (3)
Kd	0.24	0.30	0.26	0.35	0.29	0.32	0.28	0.29	0.28	0.31	0.07	0.30	0.34

Melt composition reported on an anhydrous basis. Mg# = [molar MgO/(molar MgO + molar FeO*)]×100. $\pm 1\sigma$ error reported in parentheses, based on replicate electron microprobe analyses. $\pm 1\sigma$ errors in brackets are reported as least digits cited. For example 68 (1) should be read as 68 \pm 1 wt.% and 0.6 (1) as 0.6 \pm 0.1 wt.%.

^A Estimated melt compositions by adding quench amphibole and cpx to the measured glasses of B458 and B474, respectively, until $Kd_{Melt}^{OL} = 0.3$.

^B Fe corrected

^C d melt composition due to 50% Fe loss to the Au₇₅Pd₂₅ capsule in B484.

^C H₂O concentration estimated by mass balance, assuming all H₂O in the system is dissolved in the melt. “-” indicates that the melt showed evidence of a coexisting H₂O rich fluid phase. Therefore, it could not be assumed that all H₂O is dissolved in the melt phase and H₂O concentrations by mass balance could not be estimated.

$$1210 \quad {}^{\text{D}}\ Fe - Mg\ Kd_{Melt}^{Ol} = \frac{x_{FeO}^{Ol}}{x_{FeO}^{Melt}} \times \frac{x_{MgO}^{Melt}}{x_{MgO}^{Ol}}$$

1211 **Figure 4.** Measured major element composition of melts produced in this study on an anhydrous
1212 basis plotted against temperature. The blue dotted lines and horizontal ticks represent how melt
1213 compositions from experiments B458 and B474 would change if 3 and 9 wt.% of a metastable
1214 quench amphibole and CPX, respectively, is added back into the melt composition, respectively
1215 (see text for details). Quench phase addition vectors are left out for oxides that shift less than the
1216 error bars on the original measurements when quench phases are added back, for example TiO₂ in
1217 B474 and Na₂O in B458. $\pm 1\sigma$ error bars are based on replicate electron microprobe analyses.

1218
1219 **Figure 5.** Location the apparent fluid-saturated solidus of this study in P-T space. Fluid saturated
1220 solidi from the fertile peridotite + H₂O studies of Grove et al., (2006) – G06, Till et al., (2012)-
1221 T12, Green et al., (2010)-G10, Green et al., (2014)-G14, and Millhollen et al., (1974)-M74 are
1222 plotted for comparison. The fluid saturated solidus of Pirard and Hermann (2015) – PH15, and
1223 apparent dehydration solidus of Mallik et al., (2015)-M15 are also plotted for comparison. These
1224 two studies used hydrous sediment derive melt at a fluxing agent. Our fluid saturated solidus is in
1225 good agreement with the fluid saturated solidi of G10, G14, and M74. The anhydrous peridotite
1226 solidus is from Hirschmann (2000) – H00.

1227
1228 **Figure 6.** Comparison of partial melt compositions from this study with previous peridotite +
1229 hydrous sediment melt studies (Pirard and Hermann 2015, Mallik et al., 2016), peridotite +
1230 hydrous slab melt studies (Mitchell and Grove 2015, Grove and Till 2019) and a peridotite + H₂O
1231 study without an added slab component (Tenner et al., 2012) plotted as function of melt fractions.
1232 The starting compositions of these studies all have bulk H₂O of 2.5 – 4.21 wt.% (Table 1). All melt
1233 compositions are presented on an anhydrous basis. Vertical error bars are $\pm 1\sigma$ uncertainties based
1234 on replicate microprobe analyses, as given in Table 3. Error in degree of partial melting in this
1235 study is smaller than the data points and are given in Table 3.

1236

1237

1238

1239

1240

1241

1242 **Figure 7.** Left side: SiO_2 concentration on an anhydrous basis vs. temperature of melts produced
1243 via hydrous peridotite melting from 1-3.5 GPa. Right side: Degree of partial melting as a function
1244 of temperature of melts produced via hydrous peridotite melting from 1-3.5 GPa. These graphs are
1245 broken into three panels, 1-1.6, 2-2.5, and 3-3.5 GPa, corresponding to melting in the shallow
1246 mantle wedge near the moho, the hot core of the mantle wedge, and the base of the mantle wedge
1247 near the slab/wedge interface, respectively. The colorbar shows the bulk H_2O in each experiment
1248 and ranges from 0 to 6 wt. % H_2O . Data with red borders represent fluid-saturated melts, while
1249 data with black borders represent fluid-undersaturated melts. The distinction between rock types
1250 is based on SiO_2 and alkalis (TAS diagram) and does not account for similarities or differences
1251 between experimental melts and natural arc lavas in terms of other major oxides. However, it
1252 should be noted that our melt along with the melts from Mallik et al., 2015 & 2016 in the picro-
1253 basalt field would be classified as basanites on to a TAS diagram and based on the classification
1254 of Le Bas (1989). Error in the degree of partial melting is smaller than the symbol.

1255
1256 **Figure. 8** Major element data of natural arc lavas and experimentally produced melts on an
1257 anhydrous basis. Natural lavas (grey circles) are compiled from PetDB (Aegean, Aeolian,
1258 Cascades, Central American Volcanic Province, Izu-Bonin, Mariana, Sunda and Tonga) and
1259 corrected for fractional crystallization until in equilibrium with Fo_{92} . Red circles are primitive
1260 andesites and basaltic andesites compiled in Mitchell and Grove (2015). Squares are the
1261 experimental melts from this study. Diamonds are experimental melts from the peridotite +
1262 hydrous sediment – derived melts from Pirard and Hermann (2015) and Mallik et al.,
1263 (2015&2016). Hexagrams are experimental melts from the peridotite + H_2O + alkalis studies of
1264 Mitchell and Grove (2015) and Grove and Till (2019). Stars are experimental melts at 3.5 GPa
1265 from Tenner et al., (2012). Note that differences solely in pressure during fluid-undersaturated
1266 melting can account for the first order spread and diversity of natural primitive basaltic andesites
1267 to picrobasalts, where fluid saturated melting at all pressures generates primitive andesites and
1268 dacites.

1269

Figure 1

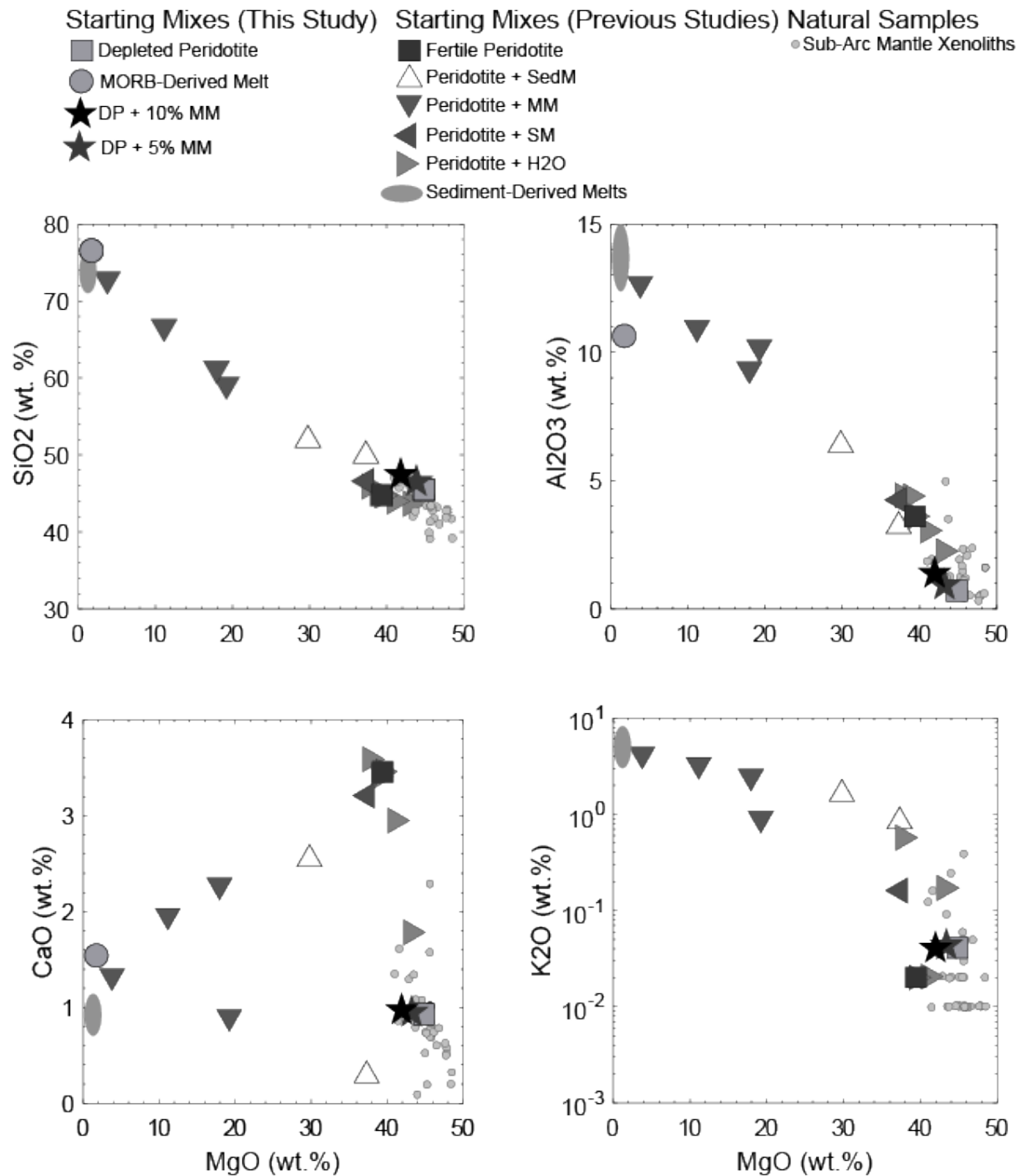


Figure 2

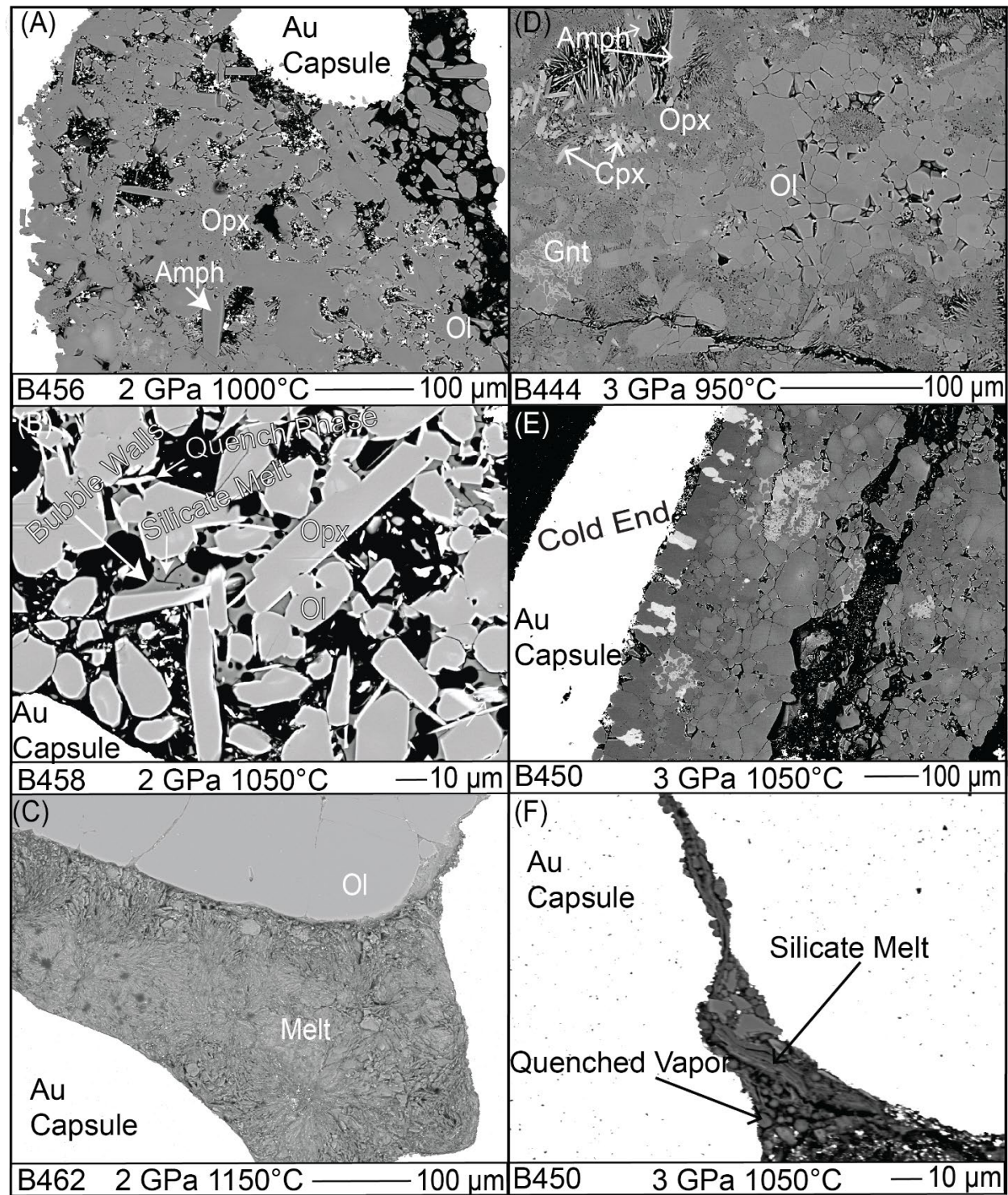


Figure 3

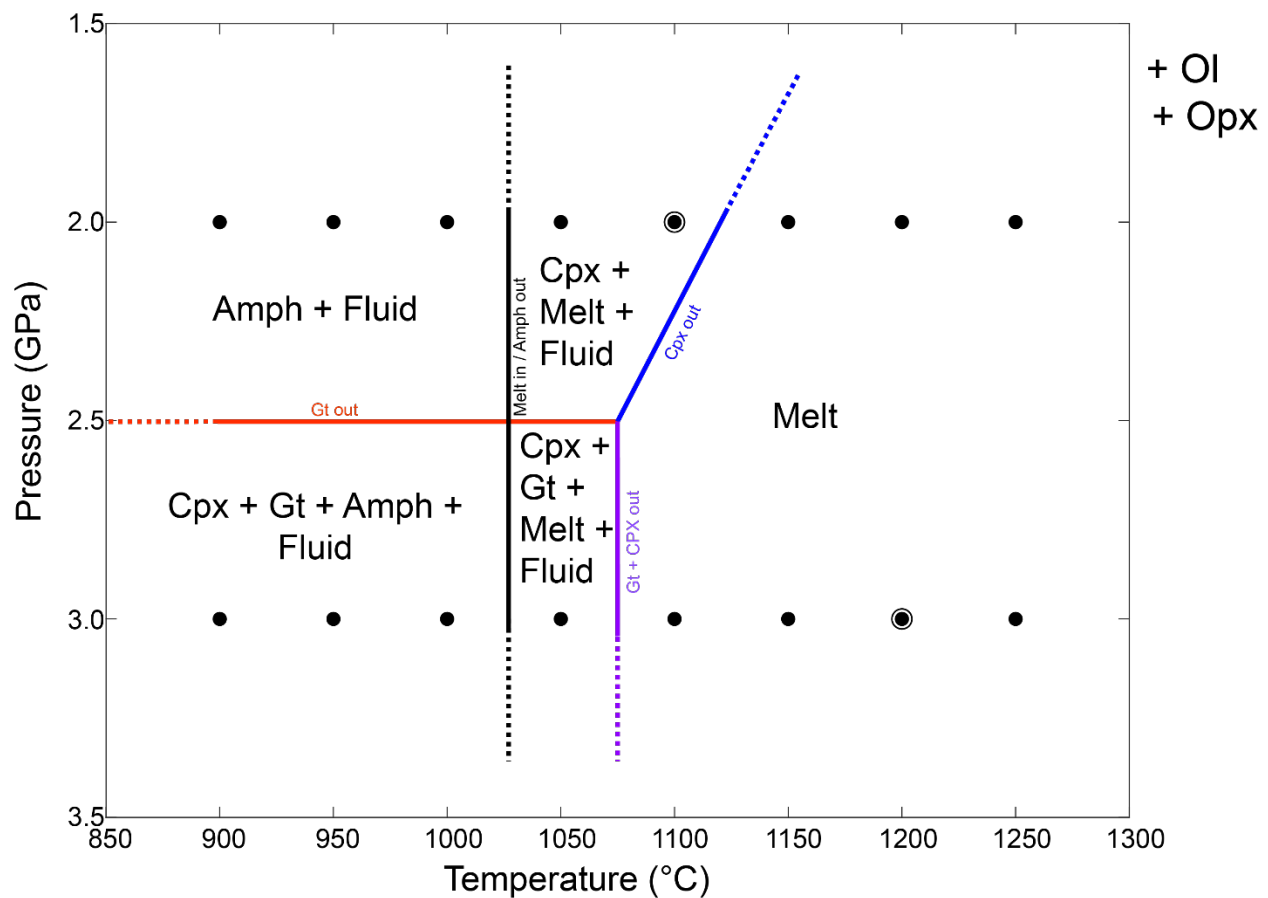


Figure 4

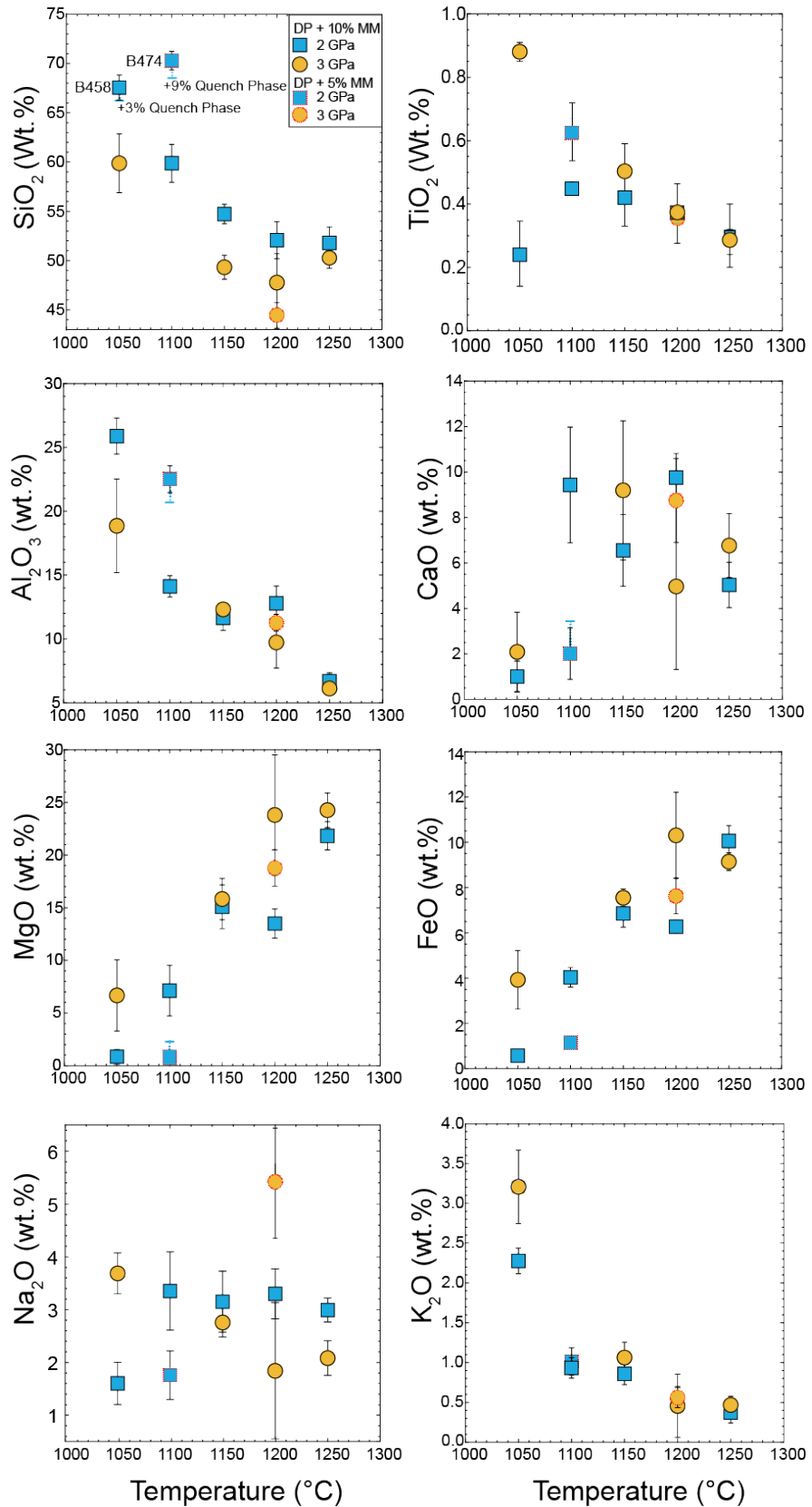


Figure 5

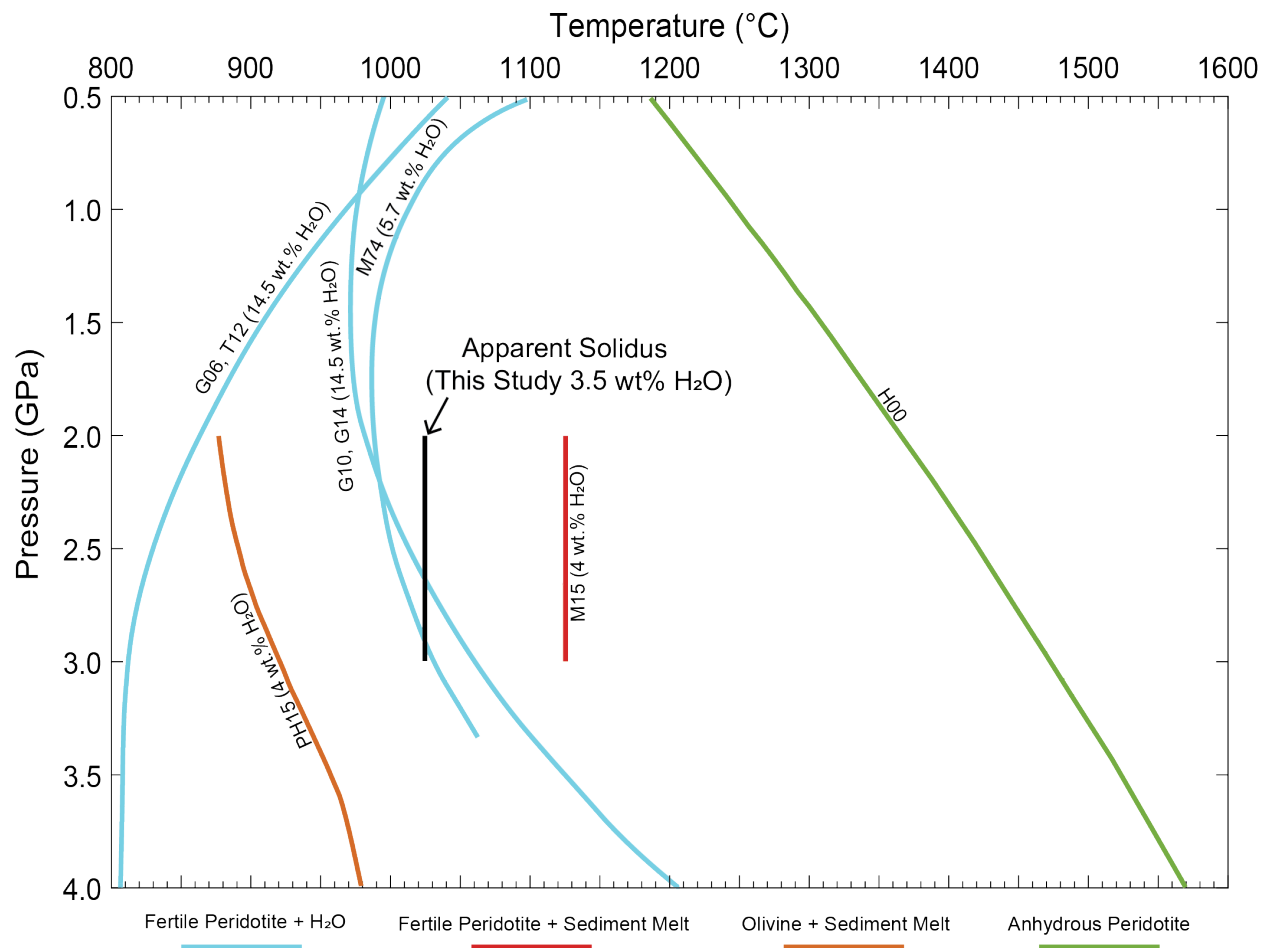


Figure 6

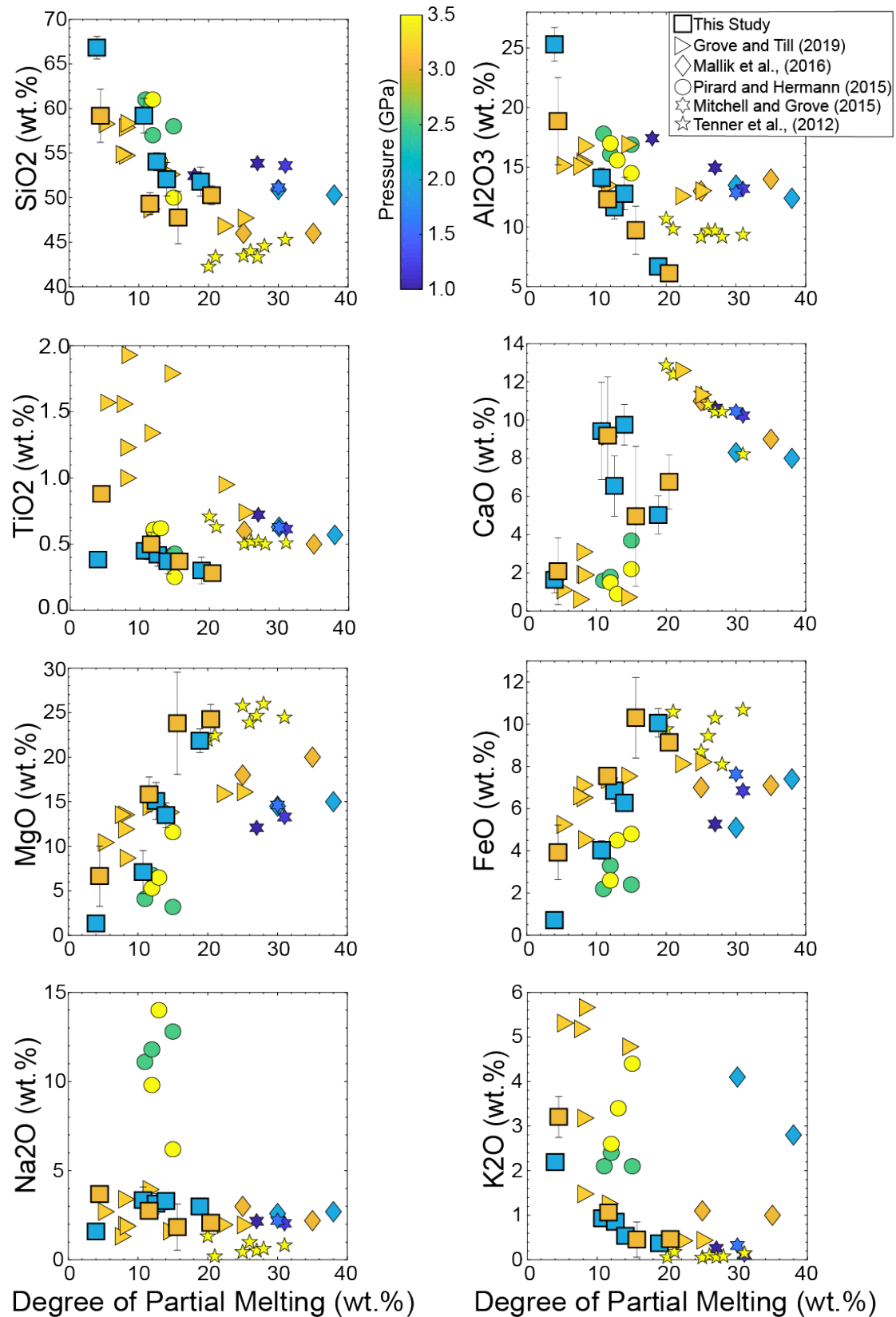


Figure 7

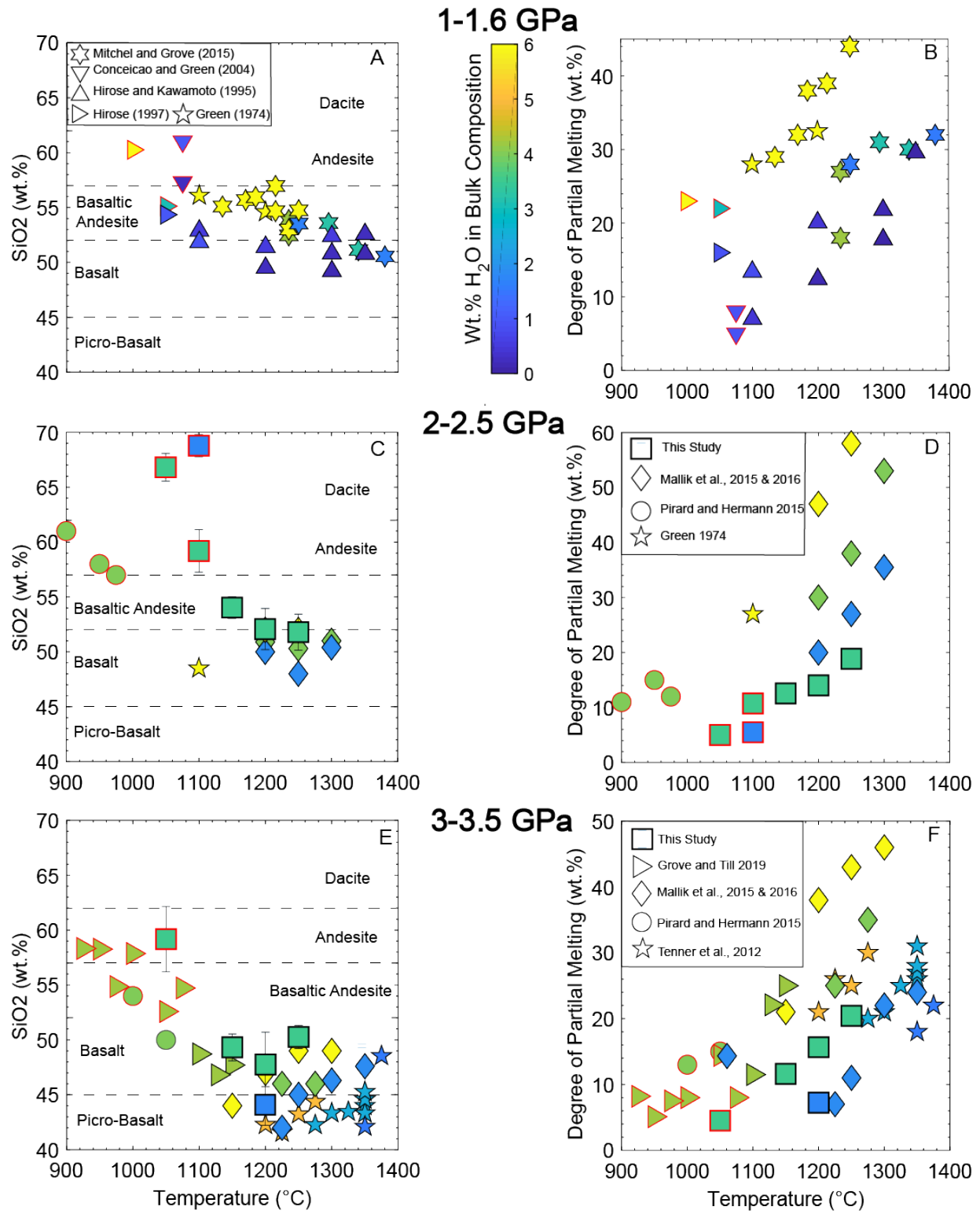


Figure 8

